OPTICAL MEASUREMENT OF NEURAL ACTION POTENTIALS USING LOW COHERENCE HETERODYNE INTERFEROMETRY

by

Mark Changhao Chu

B.Sc. (Physics) University of California at Berkeley (2001)
B.Sc. (Astrophysics) University of California at Berkeley(2001)

Submitted to the Department of Physics
in partial fulfillment of the requirements for the degree of

Master of Science in Physics

at the

MASSACHUSETTS INSTITUTE OF TECHNOLOGY

September 2004

Author .....
Department of Physics
August 6, 2004

Certified by .....
Michael S. Feld
Professor
Thesis Supervisor

Accepted by .....
Thomas J. Greytak
Associate Department Head for Education

OPTICAL MEASUREMENT OF NEURAL ACTION POTENTIALS USING LOW COHERENCE HETERODYNE INTERFEROMETRY

by

Mark Changhao Chu

Submitted to the Department of Physics
on August 6, 2004, in partial fulfillment of the
requirements for the degree of
Master of Science in Physics

Abstract

We present a novel non-invasive optical method for detection of neural action potentials using low coherence interferometry. The dual beam heterodyne interferometer (DBHI) is a modified Michelson with a low coherence source and an optical referencing method capable of detecting sub-nanometer optical path changes. In this interferometer, acousto-optical modulators were used to produce an interfering heterodyne signal between the sample and a nearby surface. To cancel the noise, a differential phase measurement was made between this heterodyne signal and a stable reference heterodyne. DBHI has a stability of 30 picometers over 100ms.

We have used this interferometer to measure the expansion of the nerve surface during the action potential. We have measured a displacement of 2-6nm using the nerves from the walking leg of a lobster. A correlation experiment showed that the optical phase signal (the swelling) from the axon during action potential can be identified with the electric signal from the extracellular electrophysiology.

A dual-beam probe was designed and built based on this interferometer. The probe is a fiber optic unit with an integrated referencing surface. The probe simplified the data taking process as well as improved the overall S/N ratio by 10 times. The compactness of the probe will allow us to obtain full field phase images with high precision and good maneuvering capability. It will be used in future studies of the action potential.

Results from the nerve experiment together with the addition of this probe indicate that DBHI is a promising instrument for studying in-vitro neural activity as well as other biophysical applications, such as the study of cochlear dynamics.

Thesis Supervisor: Michael S. Feld
Title: Professor

Acknowledgments

First and foremost, I would like to thank my mother. Though no reason is ever needed to thank a mother, I would like to thank her for her belief in me and her always optimistic spirit. I might be a white paper with some black spots, but I'll always be her paper.

I want to thank uncle and ashen for always treating me as a part of their family. Maxima work great in the snow! To all three of my sisters– Monica, Sharon and Toni(in no order of importance), I can't express enough love for you all even if I seem to live on Mars most of the time.

I would like to give big hugs and kisses to Ms. Dawn Tai, aka. "my-luh". She helped me in more ways than one in finishing the thesis since day one. I owe it for her endless support, occasional dinner, and impeccable photoshop skills. gua gua...

People in MIT: Professor Michael Feld, Ramachandra, Andrew Ahn, Gabbi, Hide Iwai, Taka, Keisuke Goda and of course Chris Fang-Yen for having the patience to guide me these years.

Lastly, none of my physics accomplishments would be possible without my 8th grade math teacher- Mr. Papoula, my high school physics teacher- Mr. Burns, or a person inspired me in many ways -Mr. Alexei Fillippenko.

Contents

List of Figures

List of Tables

Chapter 1

Introduction: Neuroscience and interferometry

"To know the brain... is equivalent to ascertaining the material course of thought and will, to discovering the intimate history of life in its perpetual duel with external forces."

-Santiago Ramón y Cajal, *Recollections of My Life* (1937), describing why the study of the nervous system attracted him "irresistibly" in the 1880s

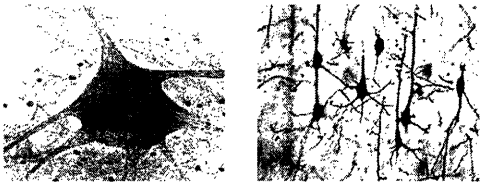

Figure 1-1: Neurons in the rat hippocampus

In 1952, a series of papers by Hodgkin and Huxley quantified how neurons communicate. They produced a mathematical model of the *action potential.* Action potentials are the underlying electrical signals generated by neurons. Perhaps understanding and tracking the neural action potentials will permit an access to the consciousness. Hodgkin and Huxley won the Noble Prize in Physiology in 1963.

1.1 Introduction

In this chapter, we will first introduce the concept of interferometry and its applications in biology. A brief discussion of action potential is then given. Finally, we present some of the effects associated with the action potential of a nerve. We will also discuss the motivation and advantages behind using low coherence interferometry in neuroscience in this chapter.

1.2 Interferometry

Using optical methods to study neurons offers many advantages over mechanical or extracellular recording techniques: a pure optical method would be non-invasive; it would be possible to image many neurons at once; light can probe mechanically inaccessible areas or very small features of neurons, such as dendrites. However, neural studies often require measuring sub-micron or even nanometer scale dynamics. Yet, this type of signal is unable to be detected via optical intensity measurements. Many microscopy methods, such as phase contrast or fluorescence, uses contrast agents to distinguish such small changes. However, any microscopy technique will be diffraction limited and mostly non-quantitative.

The Rayleigh criterion indicates that the resolution of any intensity measurement is on the order of the wavelength. However, a phase measurement is only limited by shot noise. With proper experimental design, it is possible to measure distance changes equal to fractions of a wavelength. Interferometry is the most sensitive way to measure such a change. LIGO, (Laser Interferometer Gravitational Wave Observatory) for example, uses kilometer long arms in the interferometer in an attempt to pick up length changes as small as 10^{-16} meters caused by space time disturbances of the gravitational waves. In our nerve experiment, a sub-nanometer precision is sufficient. However, the main challenge in any interferometer is to overcome phase noise. Chapter 3 will introduce the method we have used to cancel the noise based

on optical referencing.

Low coherence interferometry (LCI) is an interferometry using broadband light as source. A broadband source has a short temporal coherence length. This allows us to depth select the signals within that range, a process known as coherence gating. Chapter 2 will describe the principle behind LCI and details of the depth gating. LCI is not a novel idea, nor is the application of LCI in biology. Optical coherence tomography (OCT) is a widely used medical technique (especially in ophthalmology, due to the transparency of ocular structures) that utilizes low coherence light to obtain cross sectional microscopic in-vivo images of tissues. The advantage of OCT is that it has a high probing depth in scattering media, has a contact-free and non-invasive operation, and has the possibility to create various function dependent image contrasting methods.

However, while OCT can obtain few-micron resolution images, the neural signals in our experiment are nanometers or less. Our interferometer needs to go beyond OCT and measure the phase shifts on the scale comparable to the displacement associated with the neural signal. Moreover, it requires a noise level lower than nanometers to be able to resolve the signal without signal averaging. Chapter 3 will describe the dual beam heterodyne interferometer (DBHI) which proves to have such stability.

1.3 The action potential

1.3.1 Generation of action potential

If a small amount of electric current is passed into a long single nerve cell, or axon, the voltage across the membrane changes in accord with the current strength and the membrane's resistance and capacitance. For a giant squid axon, if the change induced in membrane voltage is less than $\approx$ 15mV, the response is passive. If, however, the membrane voltage is changed by more than 15mV, the membrane will be depolarized and an action potential occurs. Figure 1-3 shows the membrane voltage of the axon

undergoing action potential.

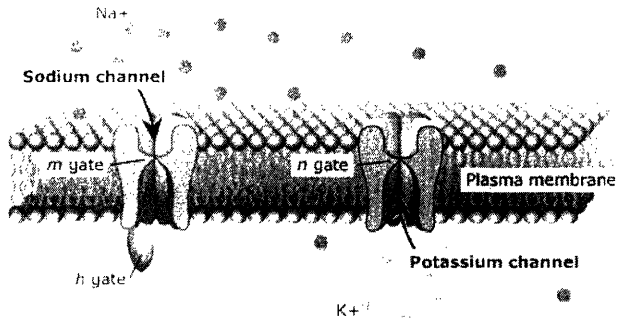

Figure 1-2: The lipid bilayer of a cell membrane at rest with the sodium and potassium ions.

On a cellular level, the action potential is a series of process between the polarization of cellular membranes and the exchange of ions. Figure 1-2 depicts the distribution of ions across a membrane of a neuron. The resting potential of this membrane depends on ratio of sodium and potassium conductances and is typically around -70mV. (Point A in Figure 1-3)

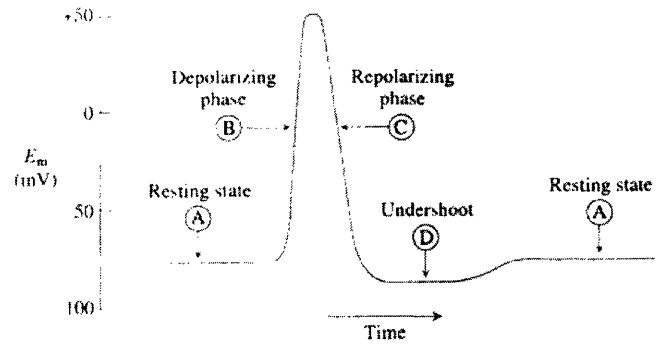

Figure 1-3: The action potential

When the cell is stimulated, the cell membrane becomes *depolarized* and the sodium (Na^+) channel will increase its conductance, allowing more sodium ions to enter. If the stimulus is too small (below the threshold), no action potential is triggered because the depolarization will also increase the potassium current (I_K). Given that exiting I_K exceeds entering I_{Na}, if there is increase in I_{Na} that is less than the

increase in I_K, then the membrane potential will return to resting value. However, at threshold, I_{Na} will equal I_K and positive feedback sets in– an action potential is initiated. (Point B in Figure 1-3) The positive feedback is between the membrane potential, the sodium conductance, and the sodium current. An increase in one will trigger an increase of the other.

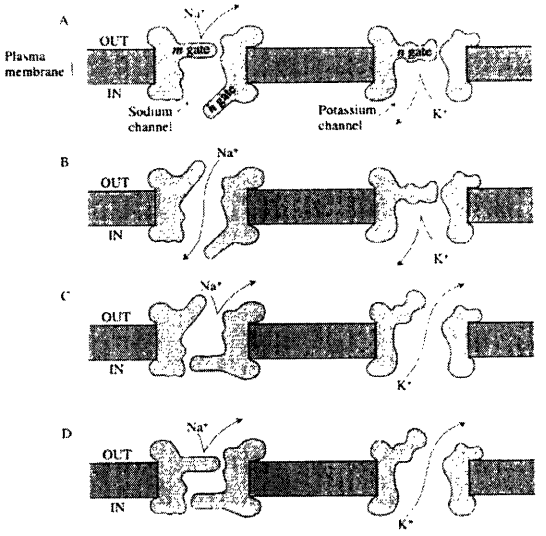

Figure 1-4: The sodium and potassium channels during action potential.

A few ms after depolarization occurs, the Na channel turns itself off and the K channel takes over. The potassium gate opens slowly with depolarization. The opening of potassium channels will pull the membrane potential back. At the peak of action potential, the potassium current will start to dominate over the sodium current. The voltage will undershoot a little bit. (Point C in Figure 1-3)

Figure 1-4 shows the two ion channels during the different stages of the action potential corresponding to Figure 1-3.

The action potential has some unique properties. First, it is an all or nothing process. The axon will not have an action potential unless it experiences stimulation beyond its threshold. Second, it is the propagation of the action potential that allows neurons to communicate. The action potential of the axon is continuously regenerated along the length of the axon so that no decrement in the strength of the signal occurs.

Third, there are many intrinsic changes associated with the action potential besides the membrane voltage.

1.3.2 Axon swelling during action potential

One of the intrinsic change associated with the action potential is the swelling of the nerve. As far as we know, the phenomenon of axon swelling during the action potential was first reported by Hill in 1950.[1] Hill studied the volume change due to stimulation of unmyelinated axons in cuttlefish, crab or lobster leg nerves. Since that time, many methods had been devised to observe the same effect.

Iwasa and Tasaki et al. published a series of report on the rapid swelling of nerves accompanied by the action potential in the 1970-1980s.[2,8,9,10] In one study of crab claw nerve, they placed a small object on top of the nerve and observed the modulation in the intensity of the light transmitted from the fiber optic source to a photodetector by the movement of that object.[9] As the nerve expands, the object on top of the nerve would partially block the light. By monitoring the intensity change, they extracted the magnitude of the upward movement of the nerve. (Figure 1-5) In another set of experiments, Tasaki *et al.* placed nanometer-diameter gold particles on a giant squid axon. They measured the change in back-reflected light intensity over 1ms period using a fiber sensor.[2] In addition to the optical methods, they also conducted an experiment using a piezoelectric transducer to measure pressure changes of the nerve.

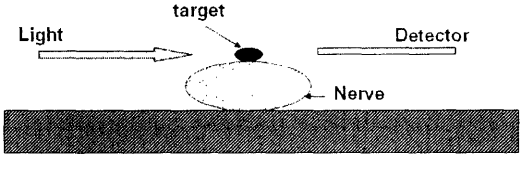

Figure 1-5: "The method of detecting a small movement of the light obstructing target on a crab nerve associated with production of action potentials" taken from *Swelling of Nerve Fibers Associated with Action Potentials* by K. Iwasa, I. Tasaki, R. Gibbons. May 1980.

The work done by Iwasa and Tasaki showed the surface displacement of the crab nerve was 5 to 10 nm in amplitude, and the pressure increase about 5 dyne/cm^2 at the peak. All three of their methods yielded similar results both in time and magnitude. These were among the first experiments that consistently showed that swelling of the nerve fiber is directly associated with the action potential. Similar results were obtained in the nerves of other crustaceans, including lobsters and crayfish. However, the origin or the swelling was speculative. Moreover, many of their result required averaging over a large data set (1000-4000 data sets). They also observed contractions, as opposed to swelling, in some of their experiments.[2]

Nerve displacements of lobsters and Nitella internodes were demonstrated using an optical lever recording by Yao, Rector and George.[4] The setup utilized a reflecting surface with opposed edges resting on the nerve and a knife-edge. A position detector recorded a signal when an incident light beam was deflected by the reflecting surface. They measured an upward displacements of less than 1nm, which is less than what Tasaki *et al.* had measured. However, since their method required putting an aluminum mirror on the sample, their result was perhaps not so surprising. A pure optical measurement free of any mechanical device suppressing the nerve's displacement would eliminate this problem. However, in these authors' own words: "These [the interferometric] methods exhibited good sensitivity, but it was difficult to adjust the preparation to obtain good interferometric fringes quickly enough for physiological recording."

A laser interferometric method was used by Hill *et al* measure rapid changes in diameter of a crayfish giant axon.[25] The phase change measured corresponded to a 1.8nm contraction of the axon surface over a period of 1 ms followed by slow swelling.

A non-contact interferometric nerve swelling experiment was reported by T. Akkin, D. Dave *et, al.*[11] Using a fiber based differential phase interferometer, they measured the transient surface displacement of a crayfish leg nerve. This system used longitudinally displaced orthogonal polarization channels to measure optical path length

change between two longitudinal points. The reported surface displacement was less than 1 nm, 1 ms in duration ,and appeared to occur simultaneously with the action potential.

One postulate of the mechanism behind the rapid mechanical change of the nerve was the idea of influx of ions during the action potential. However, Tasaki reported that "it could not be explained as the consequence of Na^+-K^+ ion exchange during the action potentials." The quantity Monovalent cations involved in the exchange is of the order of 10^{-11} mole/cm^2 per spike. The displacement attributable to this effect accounts for only 0.04 angstrom, less than 1 % of the observed displacement. Another unanswered question is whether the swelling is isovolumetric. It has been reported that the expansion of nerve fibers in the transversal direction is accompanied by a contraction in the longitudinal direction.[12] However, a measurement of hydrostatic pressure in a watertight chamber demonstrated a volume expansion in response to electrical stimulation and showed that the swelling and the shortening do not compensate each other in volume changes.[13]

Most of the techniques discussed above would be difficult if not impossible to employ in vivo. Moreover, all of the systems mentioned required extensive data set averaging. A large amount of simulation on the nerve could be detrimental to the interpreted result, since a dissected nerve has a typical activation period of 20-30 minutes and repeated stimulation could fatigue the nerve.

In this thesis, we will present a new interferometric method using low coherence interferometry to measure sub-nanometer displacements of a lobster leg nerve during the action potential. The system will prove to be fast (ms), accurate (sub-nanometer), and does not require any signal averaging. Moreover, with some development, it could be used to answer the question of volume change and to study other biophysical mechanisms responsible for the swelling.

1.3.3 Other intrinsic neural signal during the action potential

The changes in the transmembrane electric field of the action potential is $10^5 V/cm$.[3] Besides the physical swelling, this electric field alters many other intrinsic optical properties of the membrane.

Birefringence

A birefringence study of a nerve during action potential using interferometric detection in vitro was presented by A. LaPorta and D. Kleinfeld.[5] The basic setup includes a polarizer and an analyzer in crossed orientation with a nerve placed between at 45 degrees to the optical axis. Two beams prepared with orthogonal polarization came out of the interferometer was then spatially separated by a Wallaston prism. One beam will focus on the nerve and the other on a nearby point. A change in the optical density of path length of the axon during an action potential would result in a change in the combined polarized state. A peak change of 0.4 mrad was reported.

Scattering

More than 40 years ago, Hill and Keynes observed changes in the intensity of light scattering at large angles from the nerve during electrical activity.[1] Cohen also detected other optical signals in giant axons that depend on the membrane current and voltage.[18,19]

The correlation between the membrane potential and the local optical scattering properties of neurons was established by R. Stepnoski et al.[3] They used dark-field microscopy to detect scattered light from cultured neurons during stimulation and observed an optical signal that is linearly proportional to the change in the membrane potential.

S. Boppart used functional optical coherence tomography (fOCT) to detect neural activity through scattering changes.[6] For this study, Boppart *et al.* imaged the pleural-visceral connection of *Aplysia californica*. The axial resolution of their image was 2 microns. The specimen was externally stimulated and fOCT images were

acquired before, during and after stimulation at intervals. They also demonstrated that the optical scattering changes of neural tissue result from propagating action potentials.

Other effects

Tasaki over the years has measured mechanical, thermal, absorption, optical activity, fluorescence signals associated with stimulation.[21,26,27] Most of the mechanical change experiments were done using a mechano-electric transducer. The change in extrinsic fluorescence was discovered by labeling nerve fibers with probe molecules of which the emission efficiency varies with the solvent polarity.[27] Even though these properties all are means to probe the electrical activity of neurons, many of the methods used are invasive (dyes, mechanical targets, gold particles).

1.4 Discussion

In the following chapters, we will introduce an optical technique using interferometry to study the swelling of the nerve during action potential. Based on previous studies, our interferometer will need to have sub-nanometer stability over the time period of the action potential ($\approx$ 20-30 ms). Moreover, for reasons discussed before, it's ideal to obtain the displacement data without signal averaging. Our dual beam heterodyne interferometer (DBHI) will satisfy all of these conditions.

Chapter 2

Experimental methods

2.1 Introduction

In this chapter, we will explain the physical principles behind the dual beam heterodyne interferometer (DBHI). We start with the concept of low coherence interferometry (LCI) and why it is needed. All of our desired signal is embedded in the phase of our interference signal. To extract the phase, we used Hilbert transforms. We will define and explain the Hilbert transform mathematically.

2.2 Low Coherence Interferometry

Low coherence interferometry refers to using a broadband light as the source. As mentioned before, this class of interferometry in biomedical context evolved into a technique generally referred to now as optical coherence tomography. OCT is used to produce cross-sectional internal structure of living tissues such as the eye, blood vessels and gastrointestinal tract.[12,14,15]

First consider a simple Michelson interferometer with a monochromatic source in Figure 2-1.

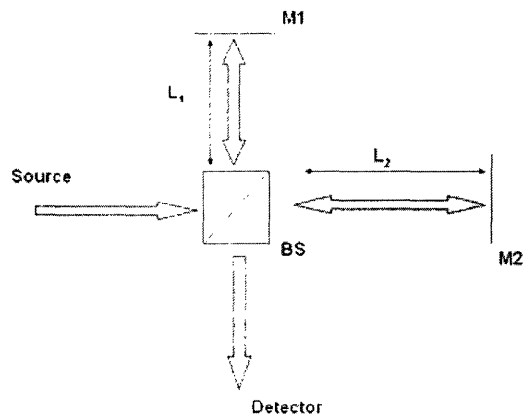

Figure 2-1: A simple Michelson interferometer. M1, M2 are mirrors. BS is a beam splitter. L_1 and L_2 are optical path lengths from the beam splitter to mirrors 1 and 2, respectively.

The field intensity at the detector is:

$$i_d =< |E_d|^2 >= I_1 + I_2 + 2\sqrt{I_1 I_2}\cos(2k_0(L_1 - L_2)) \tag{2.1}$$

where k_0 is the wavenumber of the source and I_1 and I_2 are the mean (dc) intensities returning from the two arms of the interferometer. The cross term on the right hand side in the equation depends on the optical delay set by the position of the two mirrors. If instead of a fixed mirror, we replace M2 with a tissue that has small scale motions in time ($L_2(t)$), then the cross term in the above equation will carry information

about the tissue structure/dynamics. Various OCT techniques have been devised to modulate L_1 to separate the cross-correlation signal from the dc component of the intensity to extract such information.

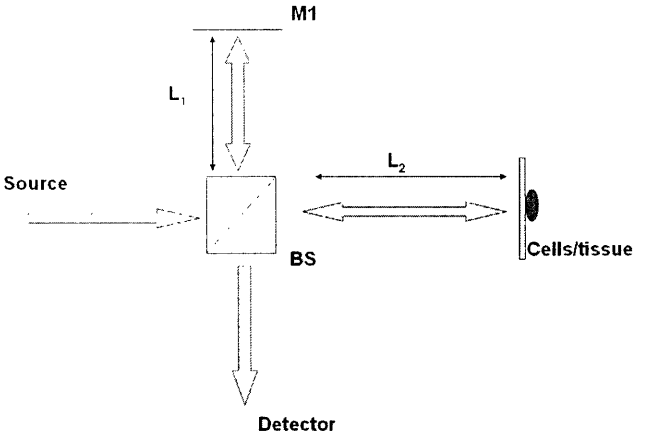

Figure 2-2: A simple Michelson interferometer with cells on one arm. BS is a beam splitter. L_1 and L_2 are optical path lengths from the beam splitter to mirrors 1 and cell.

However, we cannot use this simple setup with a monochromatic source to measure nanometer changes of the sample. The instabilities (vibrations) of the optics in the interferometer alone give rise to a noise on the order of microns. Moreover, even if we stabilize the interferometer down to nanometer accuracy, all the stray reflections from our optics and from unwanted scattering signals from different layers of the cell will contribute to i_d. The detected intensity will be a mixed bag of signals. In our example, it will be very difficult, if not impossible, to separate out the cell dynamics in question.

The use of a broadband light source solves that problem. The broadband source is desirable because it produces interference patterns of short temporal extent. To get the AC term in Equation 2.1, we will have to integrate Equation 2.1 over the coherence characteristics of the source.

$$i_d = \int I(\nu)S(\nu)d\nu \tag{2.2}$$

According to the Weiner-Khinchin theorem, $G(\tau)$, the complex temporal coherence function of the source, is related to S(ν), the power spectral density of the source, by

$$G(\tau) = \int_0^\infty S(\nu) \exp(-i2\pi\tau) d\nu \tag{2.3}$$

where τ is the optical time delay set by the relative positions of M_1 and M_2. Thus from Equations 2.2 and 2.1, the detected intensity is:

$$i_d =< |E_d|^2 >= I_1 + I_2 + 2\sqrt{I_1 I_2}|G(\tau)| \cos(2k_0(L_1 - L_2)) \tag{2.4}$$

If the power spectral density of the source is:

$$S(\nu) = \frac{2\sqrt{\ln 2/\pi}}{\Delta\nu} \exp[-4 \ln 2(\frac{\nu - \nu_0}{\Delta\nu})^2] \tag{2.5}$$

then

$$G(\tau) = \exp[-(\frac{\pi\Delta\nu\tau}{2\sqrt{\ln 2}})^2] \exp(-i2\pi\nu_0\tau) \tag{2.6}$$

From the above equation, we can define a coherence length l_c which equals the FWHM of the coherence function as shown in figure 2-3. Other definitions give similar expressions up to a constant.

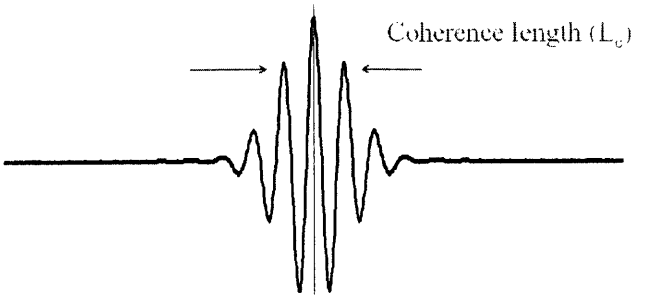

Figure 2-3: FWHM of an interferometric fringe from a single reflecting surface

$$l_c = \frac{2c\ln 2}{\pi} \cdot \frac{1}{\Delta\nu} \approx 0.44\frac{\lambda_0^2}{\Delta\lambda} \tag{2.7}$$

Thus if $\Delta L = L_2 - L_1$ is larger than l_c, there will be no interference between the signals from the two arms. In other words, any reflections in the interferometer separated by an optical distance larger than l_c will not contribute to the interference term. This depth selectivity thus eliminates unwatned contributions to the interference signal and confines the signals that can contribute to within the coherence length of the source.

2.3 Low coherence heterodyne signal

As with many OCT designs, it is preferable to modulate the sample signal to separate out the DC and AC components. A common technique used in OCT is to modulate the reference mirror (M1 in figure 2-1). In our experimental design, we instead send the light to two acousto-optic-modulators (AOMs) operating at two slightly different frequencies. The recombined light will create a heterodyne interference signal at a frequency low enough to be detectable by a photodiode.

2.4 Extracting the phase: Hilbert transform

In general, there are many methods, both experimental and analytical, to extract the phase of a heterodyne signal. The Hilbert transform is used widely to obtain the phase of the signal. Here we give a brief mathematical description of it.

Consider a following signal g(t) from which we would like to extract the phase (ϕ):

$$g(t) = \cos(\omega t - \phi) \tag{2.8}$$

The idea is to convert g(t) to a form of G(t)= $e^{\Phi(t)}$,where $\Phi(t) = i(\omega t - \phi)$. Then the heterodyne phase can be calculated via:

$$\Phi(t) = \begin{cases} \tan^{-1}(\frac{Im\ G(t)}{Re\ G(t)}) & \text{if } Im\ (\mathrm{G(t)}) > 0, \\ \tan^{-1}(\frac{Im\ G(t)}{Re\ G(t)}) + \pi & \text{if } Im\ (\mathrm{G(t)}) < 0 \end{cases} \tag{2.9}$$

The way we do this is by using Hilbert transform. The Hilbert transform of a function g(t) is defined by

$$H(x) = \frac{1}{\pi} \int_{-\infty}^{\infty} \frac{g(t)}{x - t} dt \tag{2.10}$$

by a change of variable, we can rewrite Equation 2.10 as

$$H(x) = \frac{1}{\pi} \int_{-\infty}^{\infty} \frac{g(x - t)}{t} dt \tag{2.11}$$

or

$$H(x) = -\frac{1}{\pi} \int_{-\infty}^{\infty} \frac{g(x + t)}{t} dt \tag{2.12}$$

H(x) is thus a convolution:

$$H(x) = \frac{1}{\pi x} * g(x) \tag{2.13}$$

From the convolution theorem:

$$F(H(x)) = F(\frac{1}{\pi x}) F(g(x)) \tag{2.14}$$

where F is the Fourier transform.

In the example, the Hilbert transform of g(t) is $\sin(\omega t - \phi)$ and we can simply create G(t) by

$$G(t) = g(t) + iH(x) \tag{2.15}$$

This is true in general: for a real function g(t), we can associate a complex function by having g(t) as the real part and the Hilbert transform of g(t) as the imaginary part.

Another recipe for doing the Hilbert transform is by a series of Fourier transforms. The steps are: Fourier transform g(t); filter out the negative frequency component; and then Fourier transform the remaining signal back. We would then obtain the $e^{i\Phi(t)}$, from which we can extract the phase via Equation 2.9.

Chapter 3

Dual beam heterodyne interferometer (DBHI)

3.1 Introduction

After a discussion on the physical principles behind the DBHI, we will now be to discuss the parts and pieces of the experimental setup. We will start with the electrically referenced phase canceling technique, and then move to a more elegant optically referenced method. We will present a proof of principle experiment as well as an evaluation of the stability level of the system.

3.2 Overview of the DBHI

The dual beam heterodyne low coherence interferometer is shown in Figure 3-5. This interferometer is used to measure phase changes of reflected light from a sample relative to a reflective surface above (or below, depending on optics geometry, see Figure 3-1).

A low coherence source (Optospeed Superluminescent diode SLED155020a; center wavelength 1550nm; FWHM 35nm) is coupled into a single mode optical fiber which

enters a Michelson interferometer. Each of the two arms in the interferometer contain acousto-optic modulators (AOMs) driven by RF fields at different frequencies ω_1 and ω_2. We use a pinhole to select the first order diffracted beam. The light is focused by the lenses onto M_1 and M_2. (Figure 3-2) The lens is placed one focal length away from both the mirrors and the AOMs. This will align all the spectrum of the low coherence light through the AOM.

If L_1 and L_2 are not equal, the light from the two paths will have a delay and form a "dual beam". In our setup, M_1 is attached to a translation stage which can give an adjustable delay of $\frac{\Delta L}{c}$ between the two beams.($\Delta L = L_1 - L_2$)

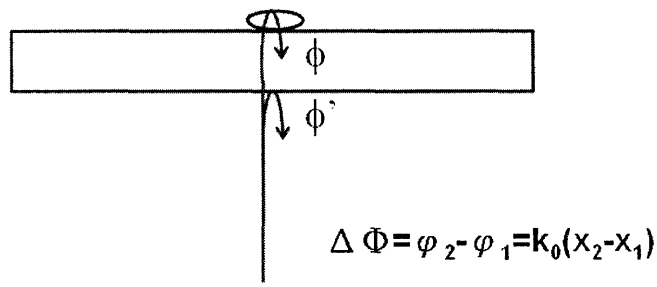

Figure 3-1: Reflection from the sample. The two surfaces have reflectivity of R_1 and R_2. x_1 and x_2 are the optical path lengths to the reflections

Figure 3-1 shows a closeup of the sample arm. Light coming out of the interferometer is collimated and focused onto the sample surface. The back scattered light from both the sample and the glass is collected. The reflection from the glass is used as the reference reflection. Let Δx be the path length difference between the light reflected off the bottom of the glass and the light reflected off the sample. (Figure 3-1) Suppose for now ΔL is zero. We would not be getting any heterodyne interference signal if Δx is larger than the coherence length of our source. Thus we would need to adjust M_1, the variable delay, such that $\Delta L = \Delta x$ to within the coherence length. When this condition is met, an interfering heterodyne signal from these two surfaces will be detected at the frequency $\Omega = 2(\omega_1 - \omega_2)$.

The phase of this heterodyne signal contains the information we are after: the phase change of the sample reflection relative to the reference reflection. We will now discuss the two methods we have used to extract the phase of this heterodyne signal.

3.3 Electrically referenced DBHI in vacuum

Our first attempt in trying to extract the phase information was to use the optical signal from the sample and reference it with the electrical driving signal of the AOMs. Furthermore, the interferometer was put inside of an air/vibration isolated chamber to actively reduce the noise in the system. Figure 3-2 shows the isolated electrically referenced DBHI setup. We will now give a mathematical description behind this method.

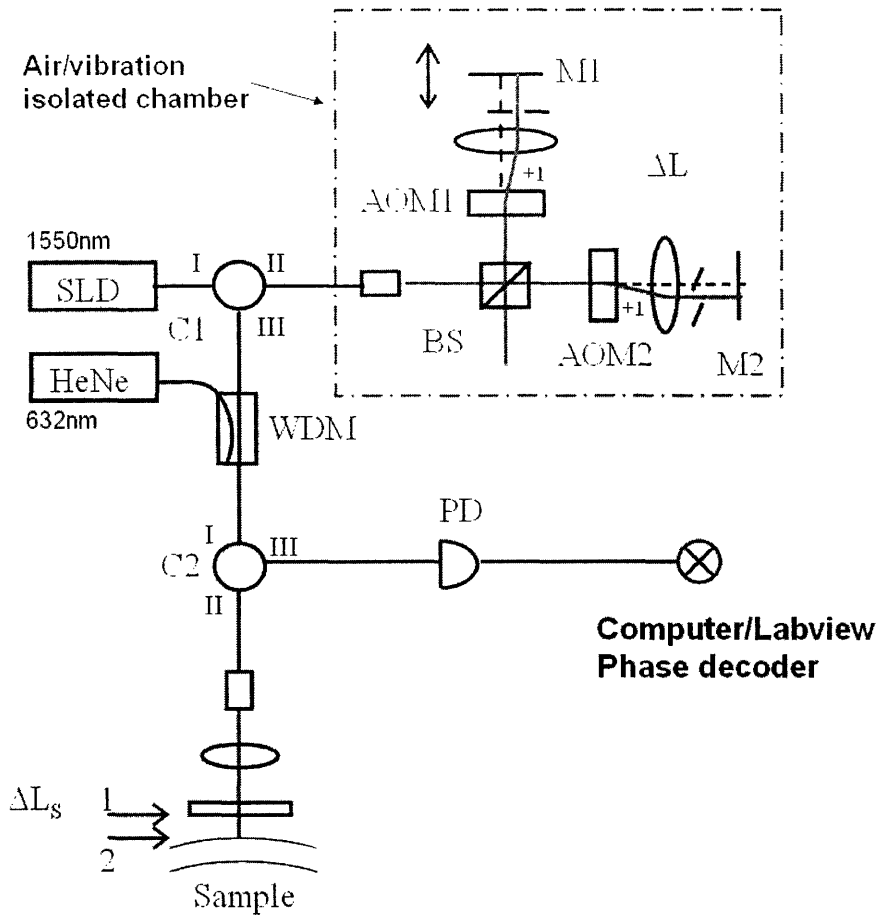

Figure 3-2: Electrical referenced interferometer setup with air/vibration isolation. SLD is superluminescent diode. M1, M2 are mirrors. AOM1, AOM2 are acousto-optic modulators. WDM is wavelength division multiplexer. C1, C2 are optical circulators. PD1 is InGaAs photodetectors. HeNe is the guide laser.

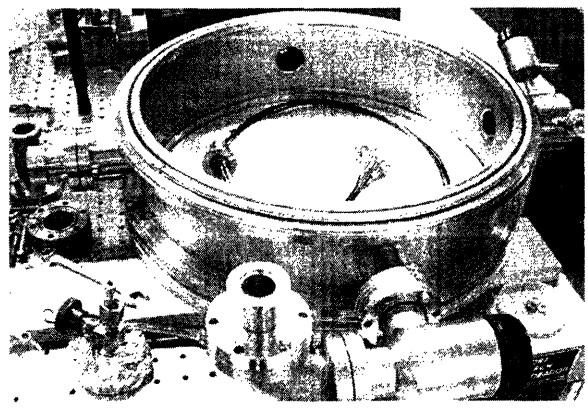

Figure 3-3: The base of the vacuum chamber used.

3.3.1 Continuous wave

Consider for now a CW source that gives an E field:

$$E = A\cos(k_0 z - \omega_0 t) \tag{3.1}$$

where k_0 and ω_0 are the wave number and the frequency of the source, respectively. After this E field passes through an AOM_i, the frequency of the field will be shifted by ω_i, the acoustic frequency of the i_{th} AOM.

Figure 3-2 has two AOMs operating at slightly different frequencies. Taking the first order beam, the field coming back from the first arm of the Michelson to the beam splitter now has a frequency of $\omega_0+2\omega_1$, and from arm 2, $\omega_0+2\omega_2$. ($2\omega_i$ because of the double pass) The sum of the two E fields is:

$$E_{output} = E_1 + E_2 = A_1\cos(2k_1 l_1 - \Omega_1 t) + A_2\cos(2k_2 l_2 - \Omega_2 t) \tag{3.2}$$

where $\Omega_1 = \omega_0 + 2\omega_1$ and $\Omega_2 = \omega_0 + 2\omega_2$.

This field is now incident on the sample similar to in Figure 3-1. If the reflectivity of reference and the sample surface are R_1 and R_2, then the field reflected from the sample is:

$$\begin{aligned} E_{sample} = {} & A\sqrt{R_1}\cos(2kl_1 + x_1 - \Omega_1 t) \\ & + A\sqrt{R_1}\cos(2kl_2 + x_1 - \Omega_2 t) \\ & + A\sqrt{R_2}\cos(2kl_1 + x_2 - \Omega_1 t) \\ & + A\sqrt{R_2}\cos(2kl_2 + x_2 - \Omega_2 t) \end{aligned} \tag{3.3}$$

where x_1 and x_2 are the optical distance to the reference and sample reflection as shown in Figure 3-1.

Square the above equation and we have the detected intensity:

$$\begin{aligned} I_{pd} \propto & (R_1 + R_2)(1 + \cos(2k_0\Delta l - \Omega t) \\ & + 2\sqrt{R_1 R_2}[2\cos(2k_0\Delta x) + \cos(2k_0(\Delta l + \Delta x - \Omega t)) \\ & + \cos(2k_0(\Delta l - \Delta S - \Omega t))] \end{aligned} \tag{3.4}$$

where we have dropped the optical frequency oscillation terms.

3.3.2 Low coherence

Using our result from the previous chapter, the spectral density of a low coherent source with a center wavenumber k_0 and FWHM spectral bandwidth Δ k is

$$S(k) = \frac{2\sqrt{\ln 2}}{\Delta k\sqrt{\pi}} \exp[-(\frac{k - k_0}{\frac{\Delta k}{2\sqrt{\ln 2}}})^2] \tag{3.5}$$

Integrating Equation 3.4 over all the spectral range gives the intensity at the detector for the low coherence case:

$$\begin{aligned} i_{detector} = \int i(k)S(k)dk = & (R_1 + R_2)(1 + \exp[-(\frac{x}{l_c/(2\ln 2)})^2](\Delta l)\cos(2k_0\Delta l - \Omega t) \\ & + 2\sqrt{R_1 R_2}[2\exp[-(\frac{x}{l_c/(2\ln 2)})^2](\Delta x)\cos(2k_0\Delta x) \\ & + \exp[-(\frac{x}{l_c/(2\ln 2)})^2](\Delta l + \Delta x)\cos(2k_0(\Delta l + \Delta x - \Omega t)) \\ & + \exp[-(\frac{x}{l_c/(2\ln 2)})^2](\Delta l - \Delta x)\cos(2k_0(\Delta l - \Delta x - \Omega t))] \end{aligned} \tag{3.6}$$

where l_c is the coherence length as defined before:

$$l_c = \frac{2(\ln 2)\lambda_0^2}{\pi\Delta\lambda} \tag{3.7}$$

If we move one of the arms of the Michelson such that the path length difference

between the two arms is exactly compensated by the different path traversed in the sample (ie. $\Delta l = \Delta x$), then the detected signal (AC) is:

$$i_{detector-ac} = 2\sqrt{R_1 R_2}[\exp[-(\frac{x}{l_c/(2\ln 2)})^2](\Delta l - \Delta x)\cos(2k_0(\Delta l - \Delta x - \Omega t))] \quad (3.8)$$

To keep Δl as constant as possible, an active noise reduction technique is implemented in this setup. We put the whole Michelson interferometer on top of a vibrational insulating stack and enclosed the interferometer in a vacuum chamber to diminish the acoustic fluctuations. Thus if we now measure the phase of $i_{detector-ac}$ relative to a local oscillator that oscillates at frequency Ω. we can measure any change in Δx.

3.3.3 Performance of this system

To measure the stability of this system, we placed a uncoated glass coverslip (reflectivity $\approx$ 4% each side) as the sample. Figure 3-4 shows the phase data taken from this experiment. In this experiment, the incident power on the sample (coverslip) is 50 μW and Ω (twice the difference frequency between the two AOM) = 200kHz.

From the data, we see a 60Hz noise and an overall drift in phase. The standard deviation of the 60Hz noise amplitude is $\approx$ 0.3 rad or 37nm in optical path length distance. This would not be acceptable for our nerve experiment. We tried to rid of the 60Hz noise by shielding, filtering, and/or different grounding techniques and we came to the following conclusions:

a)the 60 Hz noise is strictly an electrical problem that arises when the local oscillator is used as a reference to extract the phase

b)even after the 60Hz filtering, the noise level (standard deviation of 2-3nm) is still too high for the experiment

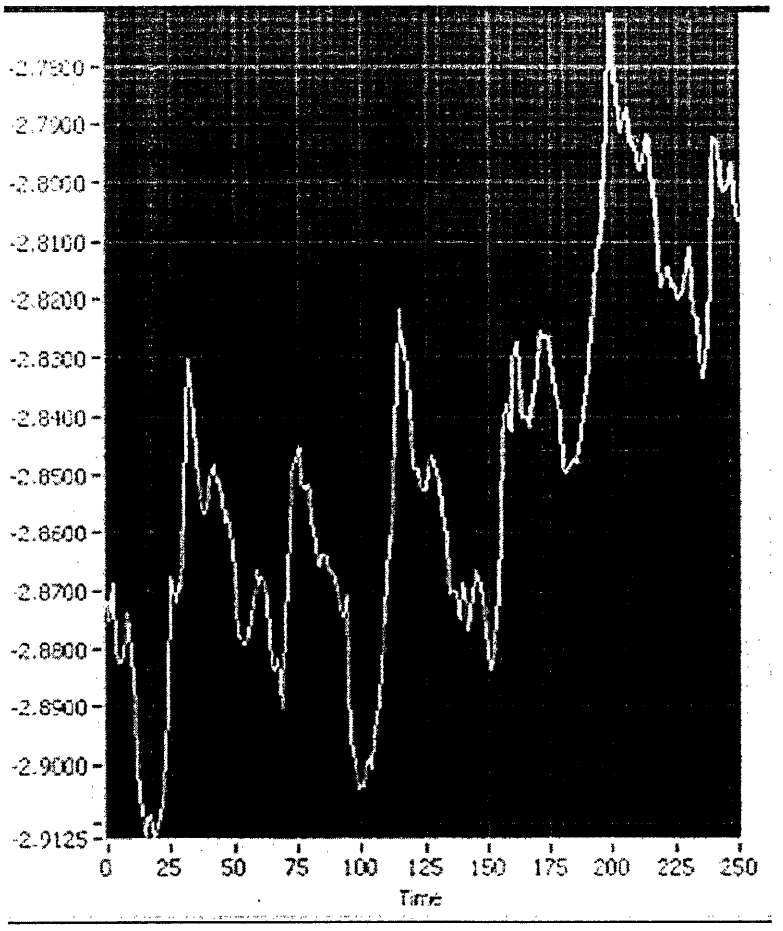

Figure 3-4: Phase change measurement of a coverslip measured using isolated electrically referenced system. Data taken over 250ms. Y axis is phase in radians.

c)enclosing AOMs in a vacuum chamber causes heating problems which directly affects our phase data

d)we are currently neglecting the second output of our interferometer thus throwing away half of the power with no compensation

These issues led to the next design, which abandons the idea of using the electrical reference and the isolated vacuum chamber. Instead, it employs the second port of the Michelson interferometer as the reference.

3.4 Optically referenced DBHI

3.4.1 Analysis

The modified setup is shown in Figure 3-5. We can apply the same result of Equation 3.8. However, instead of using the electrical driving signal of the AOMs as the reference signal and actively reduce the noise of Δl, we use the second optical output as the reference.

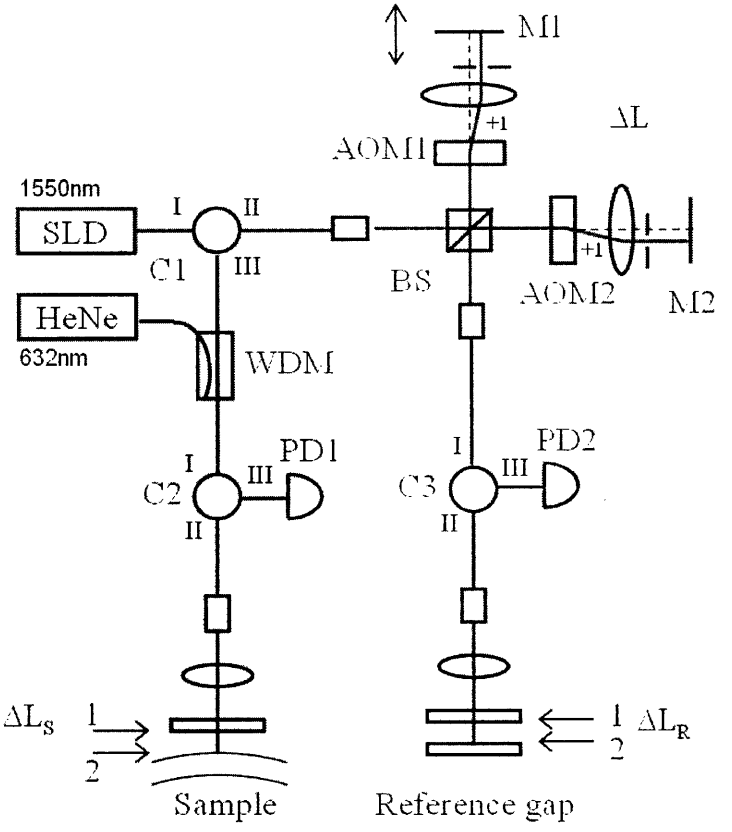

Figure 3-5: Optical referenced interferometer setup. SLD is superluminescent diode. C1, C2, C3 are optical circulators. M1, M2 are mirrors. AOM1, AOM2 are acousto-optic modulators. WDM is wavelength division multiplexer. PD1, 2 are InGaAs photodetectors. HeNe is the guide laser.

The light coming out of the second output of the Michelson goes to a reference gap. The reference gap consists of two reflecting surfaces with adjustable distance. If the optical distance difference between the two surfaces are ΔL_r, then following the

analysis in the previous section, the detected signal from the reference arm is:

$$i_{detector-ac-ref} = 2\sqrt{R_{1r}R_{2r}}[\exp[-(\frac{x}{l_c/(2\ln 2)})^2](\Delta l - \Delta L_r)\cos(2k_0(\Delta l - \Delta L_r - \Omega t))] \tag{3.9}$$

where Δl is the optical delay created in the Michelson. The detected signal from the sample arm is the same as before:

$$i_{detector-ac-sample} = 2\sqrt{R_1R_2}[\exp[-(\frac{x}{l_c/(2\ln 2)})^2](\Delta l - \Delta L_s)\cos(2k_0(\Delta l - \Delta L_s - \Omega t))] \tag{3.10}$$

with ΔL_sbeing the round trip optical path length difference between reflections from surface 1 and 2 at the sample.

We now apply the the Hilbert transform to extract the phase of the two signals and take their difference:

$$\begin{aligned} \Delta\phi &= \phi_s - \phi_r \\ &= k_0[(\Delta l - \Delta L_s - \Omega t) - (\Delta l - \Delta L_r - \Omega t)] \\ &= \Delta L_s - \Delta L_r \end{aligned} \tag{3.11}$$

Unlike the electrical referencing case, there's no longer a need to isolate the Michelson to reduce the noise on Δl down to nanometer level. This delay (Δl) and the noise associated with it is cancelled by taking the difference in phase between the sample and reference signals.

3.4.2 Performance test

In this section, we will show the fundamental stability of the system and determine its noise level. There could still be 60 Hz electrical noise, laser intensity noise, AOM

frequency drift, and maybe even shot noise. The setup is essential the same as in the previous section except there will be no PZT stages. We put a coverslip as the sample and adjust ΔL and the reference arm accordingly to obtain the heterodyne from the correct reflections. Thus now both the reference and the sample arms are Fabry-Perot cavities with the same delay. The idea is to fix everything and see how much intrinsic noise there is. The power incident on both the sample and the reference is ≈ 150 μ W.

To extract the phase, we first used a Fourier transform based phase extracting method (see Chapter 2) due to software buffer issues. After an upgrade of the data taking software LabView to 7.0, we switched to using a Hilbert transform VI (Virtual Instrument) included in the package. (See appendix for VI used) Phase wrapping is not an issue- the central wavelength of our source was 1550nm, and we're interested in studying nanometer and sub-nanometer motions.

Figure 3-6 is the result of this experiment. The figure on the left is the phase displacement on top of the coverslip, averaged over every 0.2ms. The right is averaged over every 1ms. Note, as expected, the phase data from the longer average is $\approx \sqrt{5}$ times better for a random noise.

This experiment demonstrated that the interferometer has sub-nanometer noise level over a period of 50ms. The stability of the system allowed us to perform the nerve experiment which will be presented in the next chapter.

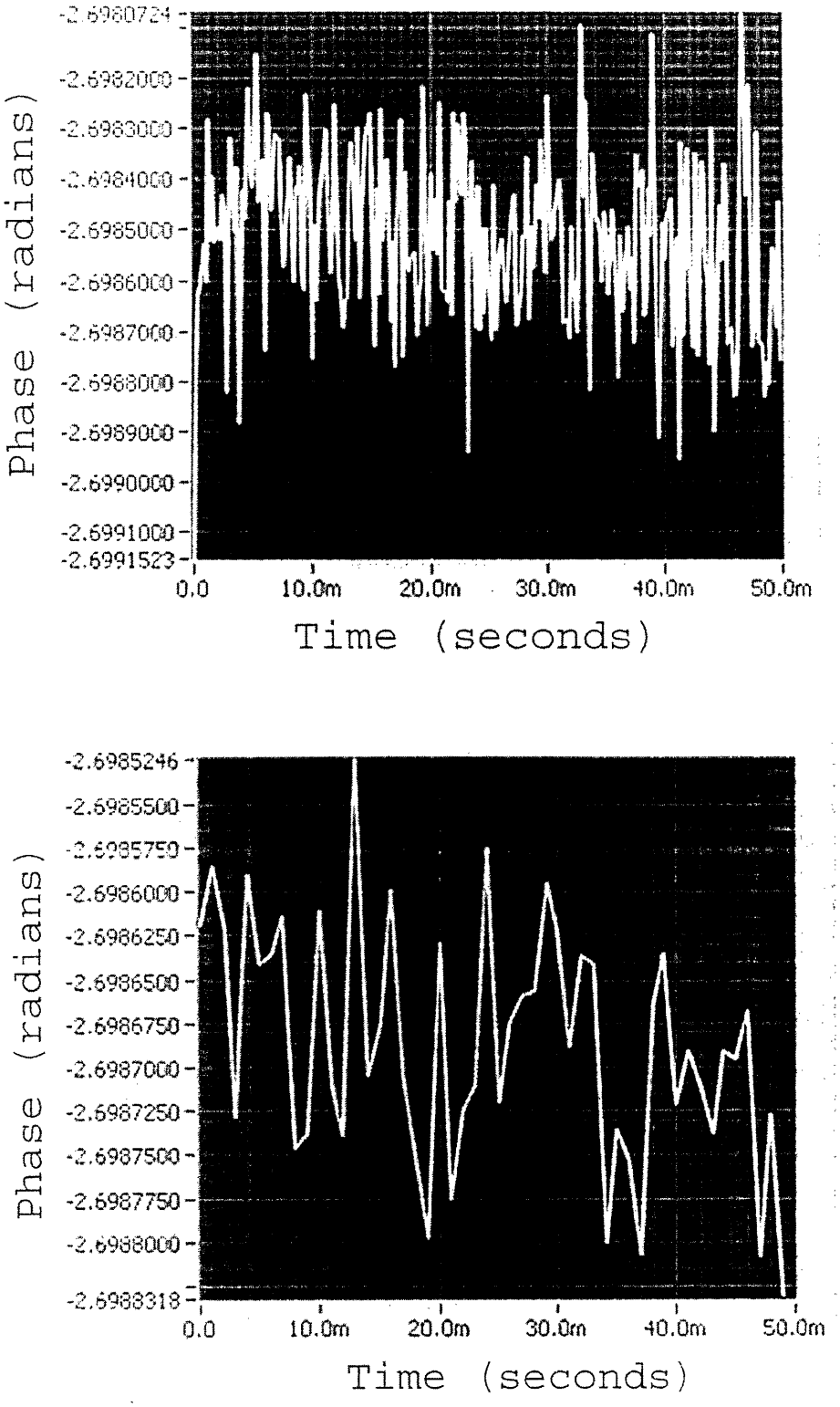

Figure 3-6: Phase fluctuation of a fixed piece of glass. Top and bottom graphs show the phase data averaged over every 0.2ms and 1ms,respectively. σ is 0.16mrad and 0.069 mrad. That stability correspond to an OPL of 40 and 20 picometers.

3.5 Calibration experiment

In this section, we wish to answer the following questions: How do we know if we are indeed measuring the phase and also how do we know if the phases we measure do correspond to the actual optical path length displacement in the sample?

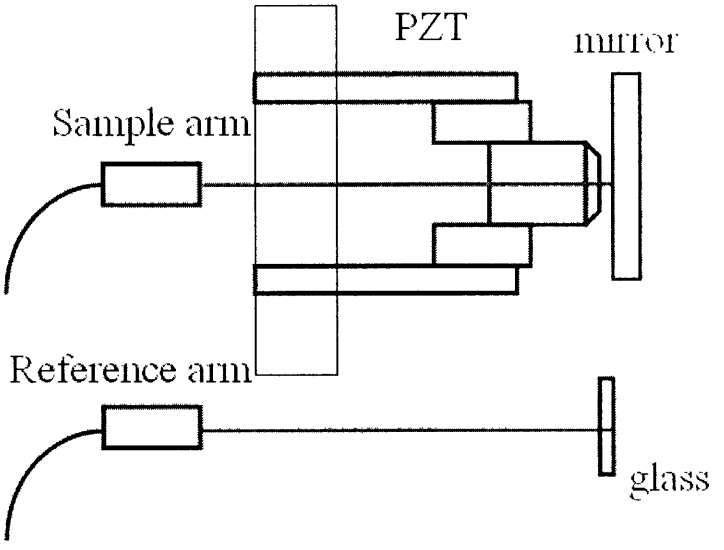

Figure 3-7: Proof of principle setup. Sample arm has a reflecting surface on PZT sinusoidal driven at 300Hz.

A proof of principle experiment was setup. The interferometer setup was the same as the optically referenced case. (Figure 3-5) The sample and the reference arms in this experiment are shown in Figure 3-7. On the sample arm, light coming out of a fiber collimator was focused on to a glass attached to the PZT stage. Once we have a good coupling of the back reflection from the glass, we aligned for the mirror reflection by adjusting the angles on the mirror mount. The fiber collimator, PZT, lens and the mirror are assembled together in a cage assembly. By systematically vibrating the mirror to known patterns and displacements, we wanted to see if our phase measurement matches them.

We drove the PZT stage with a sine wave oscillating at 300 Hz. The top and figure in Figure 3-8 is the electrical driving voltage of the PZT stage and phase measured

optically using the interferometer, respectively.

The phase data correlates with the known driven displacements of the sample mirror within $\approx$ 2 nm. The displacement of the PZT is calibrated using a HeNe (λ_0 = 632 nm). By translating M_1, we can calculate the distance moved by the number of fringes appeared via Equation 3.12. (Assuming a fringe is defined as one wavelength.)

$$\text{distance moved} = \frac{1}{2} \times \text{number of fringes} \times \lambda_0 \tag{3.12}$$

where $\frac{1}{2}$ accounts for the double pass.

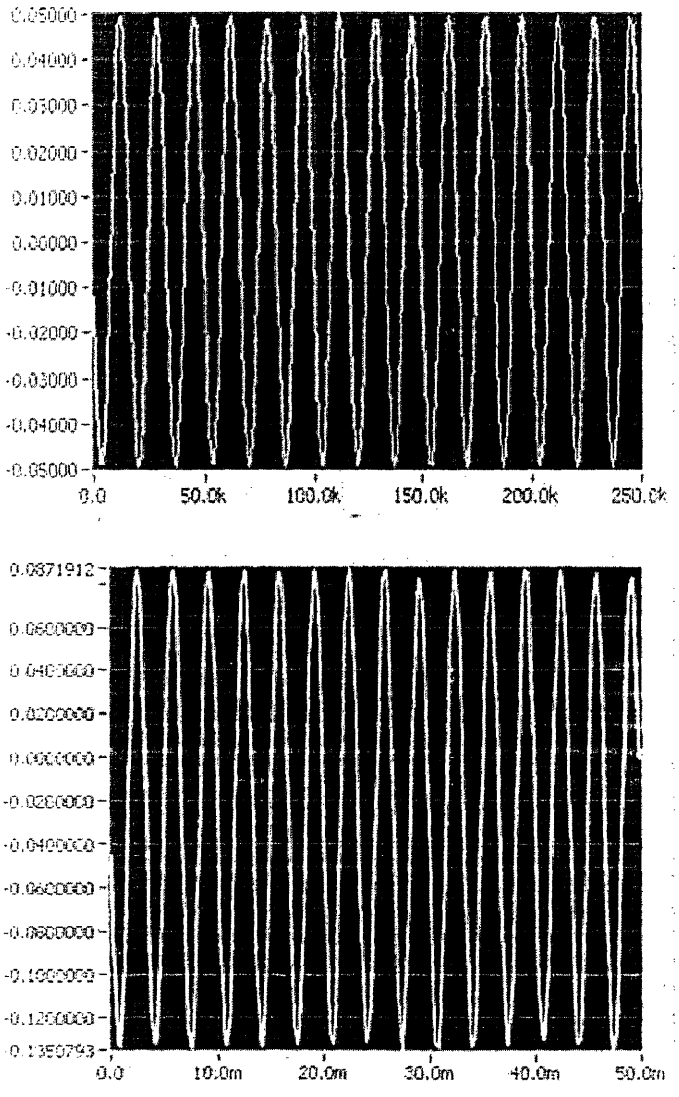

Figure 3-8: Top: Electrical driving signal of the PZT. Time in ms. Y axis is the driving voltage. 0.1V peak to peak correspond to a displacement of the PZT by 35 nm. Bottom:Sinusoidal fluctuations in phase measured using DBHI. Data taken over 50ms. Y axis is phase in radians. Peak to peak optical path length difference of 37nm.

Chapter 4

Measuring nerve displacement during action potential

4.1 Introduction

Intrinsic neural response associated with the action potential has been discussed in Chapter 1. One effect is the swelling of the nerve. We expect the signal to be on the order of nanometers or less and of about 20ms in duration from past studies[2,4,11]. Previous studies of similar experiments, however, require averaging a large data set and/or direct physical contact with the nerve. When tested using a coverslip as sample, it was shown that the noise level of this interferometer is 0.069 mrad(20 picometers in OPL). Thus, it is well capable of detecting nanometer changes in the sample. Here we will present the first non-contact optical experiment to measure such displacement.

4.2 Experimental setup

The optical setup is almost exactly as described in the previous chapter. (Figure 4-1) As with the proof of principle experiment, a Fabry-Perot cavity is used as the reference. On the sample arm, a nerve chamber is built. Refer to Chapter 3 for the details about optical setup of the interferometer. Figure 4-2 and 4-3 show the side and top view of the chamber setup.

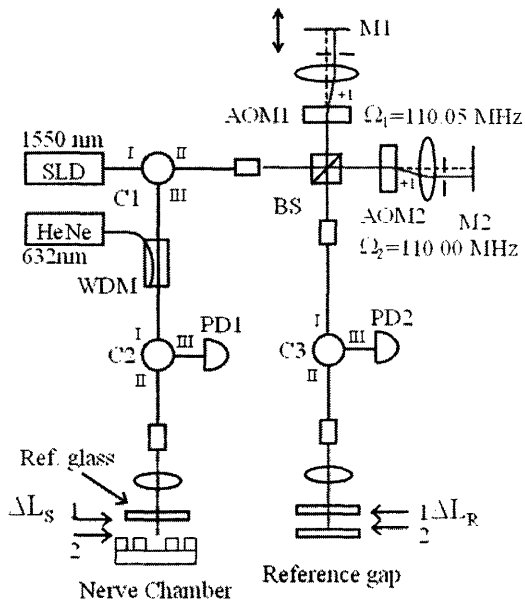

Figure 4-1: Optics setup for the nerve experiment. SLD is superluminescent diode. C1, C2, C3 are optical circulators. M1, M2 are mirrors. AOM1, AOM2 are acousto-optic modulators. WDM is wavelength division multiplexer. PD1, 2 are InGaAs photodetectors. HeNe is the guide laser.

The nerve chamber is machined out of acrylic with dimensions of 4"x1.5"x0.25" (LxWxH). The chamber contains five electrically isolated wells filled with saline solutions. A nerve from the walking leg of a lobster (*Homarus americanus*) is dissected and placed across the chamber. Petroleum jelly is then put on the nerve in regions between the wells for electrical isolation. Stimulating electrodes are placed at one end of the saline solution and the recording electrodes at the other end. The whole chamber is rested on a cage mount along with the sample arm optics.

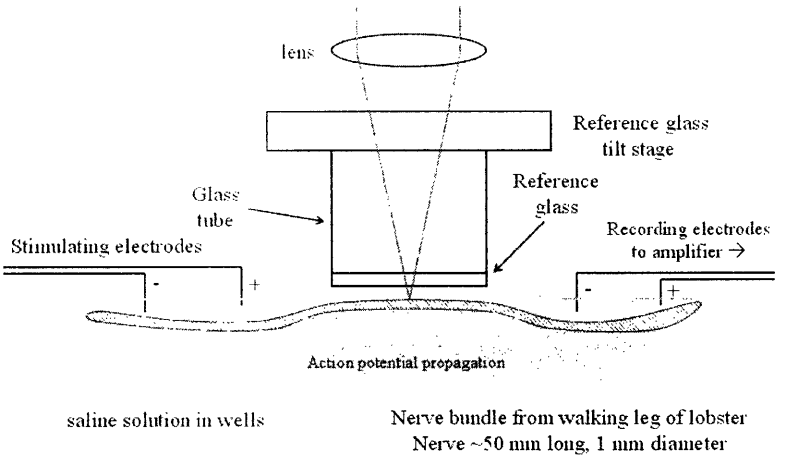

Figure 4-2: Side view of the nerve chamber setup.

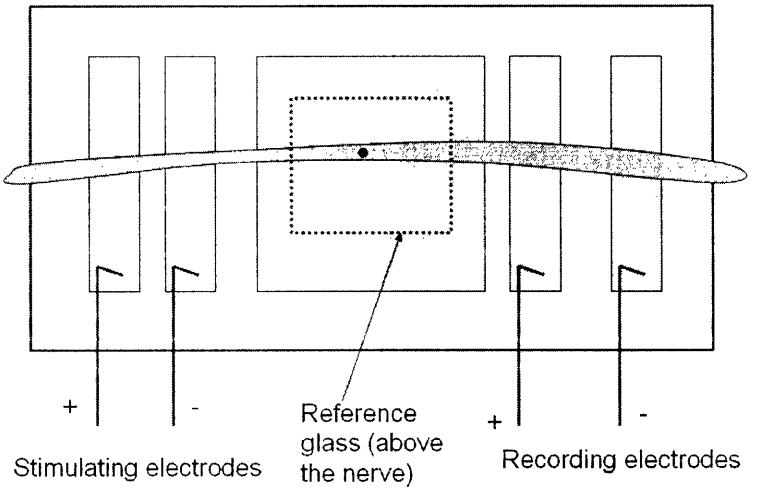

Figure 4-3: Top view of the nerve chamber setup. Red dot is the focus of the light.

On the sample arm end, light coming out of the fiber collimator (NA=0.12) is sent through a 10x telescopic system to increase the NA. The light is then focused onto the top of nerve bundle without any reference glass on top. We first maximize the DC intensity of the light reflected from the nerve. We then place the reference glass in place and note the increase of DC due to the reflection of the glass. We now have back reflecting signals from the reference glass and the nerve. However, in order to ensure that we have the correct heterodyne interference signal (since the glass has top and bottom reflections), we now scan M1 of the interferometer and note the interference

envelopes. Let ΔL_g be the optical thickness of the reference glass above the nerve Then as we move M_1 (from the position at which $\Delta L = 0$), we expect to measure three heterodyne interference envelopes. (Figure 4-4 (Central peak: $\Delta L = 0$; top and bottom glass interference, $\Delta L = \Delta L_g$; bottom glass and nerve reflection; Top glass reflection and the nerve not shown, but could be seen if we continue to scan M_1). Figure 4-4 is the data taken when we scan M_1. Note the amplitude of the peaks. Peak C is about half of peak A, as expected.

Once we have done a scan like the one shown on Figure 4-4, we move M_1 to the place where we can obtain the heterodyne signal between one surface of the glass (usually bottom side) and the nerve.

In our experiment, we stimulate the nerve by sending a square wave electrical pulse of 1ms in duration from one end. (Figure 4-5) The electrical response is then recorded at the other end. The electrical signal is then low-passed and sent through an amplifier with 10^4 gain. Both the photo detector signal and the electrical signal are sent through an A/D card (National Instruments PCI-6110: 12 bit, up to 10 MS/s/channel, up to 4 simultaneous-sampling analog inputs) to a LabView VI. Appendix A shows the control panel and the VI used to collect the data. Typical sample rate is 5 million points/sec.

For all the data shown here, the incident power on the nerve bundle is $\approx$ 70-90 μW and the heterodyne modulation is $\approx 1\mu W$.

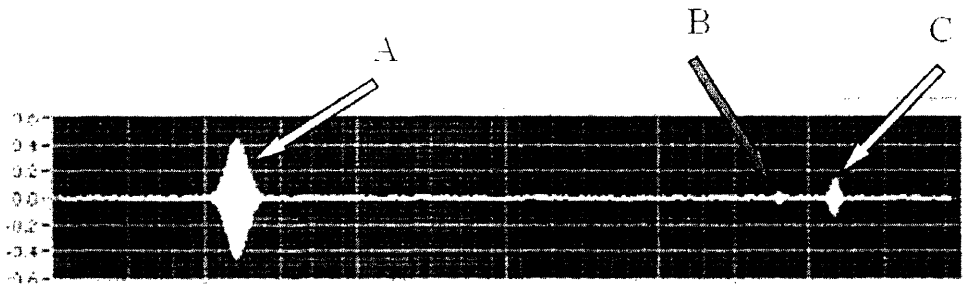

Figure 4-4: A profile of the interference signal as we change L_1 by moving the picomotor. Distance (Δ L) is displayed along the X-axis. The Y axis gives the intensity in relative units. Peak A is when $\Delta L = \Delta x$. Peak B is the interference signal between the nerve bundle surface and the bottom of the reference glass. Peak C is the interference signal between the top and the bottom of the reference glass.

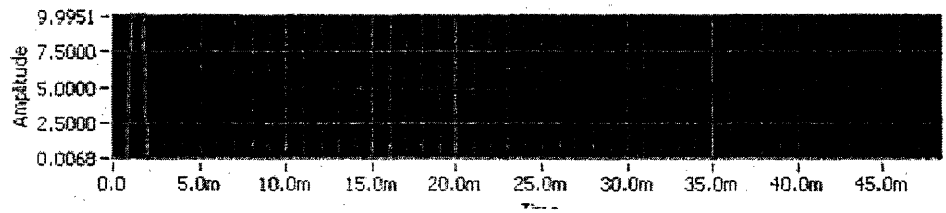

Figure 4-5: Stimulus current. 1 mA stimulation with 1ms duration.

4.3 Experimental data

4.3.1 Inactive nerve: control experiment

We want to measure the swelling of the nerve when it is undergoing an action potential. An experiment for an inactive nerve was done as a control. Figure 4-6 shows the phase and the electrical data from the nerve when it is electrically inactive. Since we are using a bundle of axons, each individual axon will have a different threshold voltage. We deem the nerve inactive when we could not notice significant electrical action potential activity when stimulated well above the typical threshold current. (1-3 mA for the lobster nerve in our experiment)

The phase data from the inactive nerve is about ten times noisier than the simple coverslip case. This is expected, since there is intrinsic motion of the nerve and the saline solution on top of the nerve surface. Moreover, the signal reflected back from the nerve is about 5-10 times lower than the coverslip experiment.

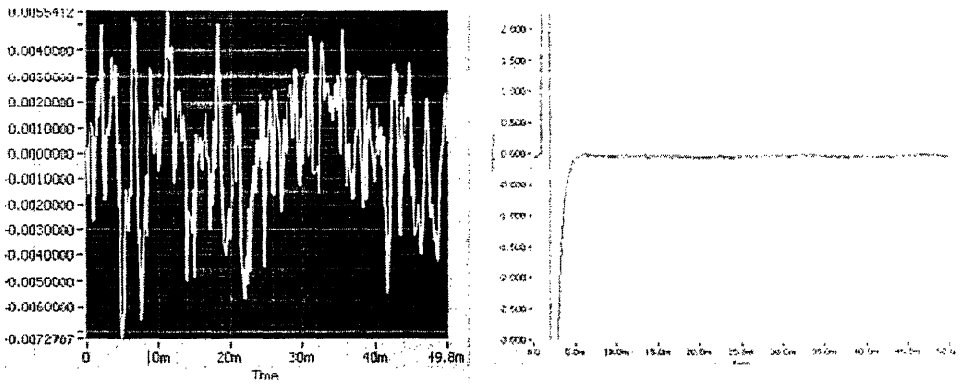

Figure 4-6: Data from an inactive nerve. No noticeable nerve displacement nor electrical potential of the nerve bundle during a 10mA stimulation. Nerve displacement Y axis in radians. Electrical potential Y axis in volts.

4.3.2 Electrically active nerve

About 70% of the nerves dissected exhibited a significant action potential. The reason for the lack of response of the rest is most likely due to errors in the dissection process. Figure 4-7 is the first ever result in this experiment. It shows phase data of an electrically active nerve. The positive phase direction corresponds to the expansion of the nerve. Note that the nerve displacement is embedded in a linear drift (evaporation of water on top of the nerve). Figure 4-8 shows the nerve displacement data after subtraction of this linear drift. (The two data are not from the same nerve, or the same lobster)

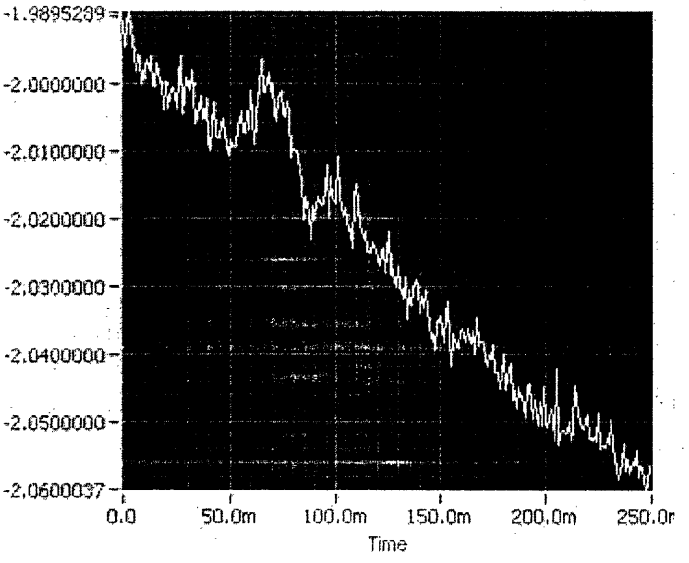

Figure 4-7: Phase change of a lobster nerve during action potential. Y axis is radians. Positive phase corresponds to an expansion of the nerve.Amplitude of expansion for this data is $\approx$ 2 nm. Linear drift likely due to water evaporation.

Figure 4-9 is the textbook graph of an action potential from a single neuron. This signal from the recording electrodes in Figure 4-8 has a stimulus artifact at time 0, followed by a series of peaks. These are compound action potential from the different axons in the nerve. The different propagation speeds of the action potential from different axons disperse. The displacement of the bundle increases as we increase the stimulus current. The maximum displacement of all the nerves ranges from 2-8 nm.

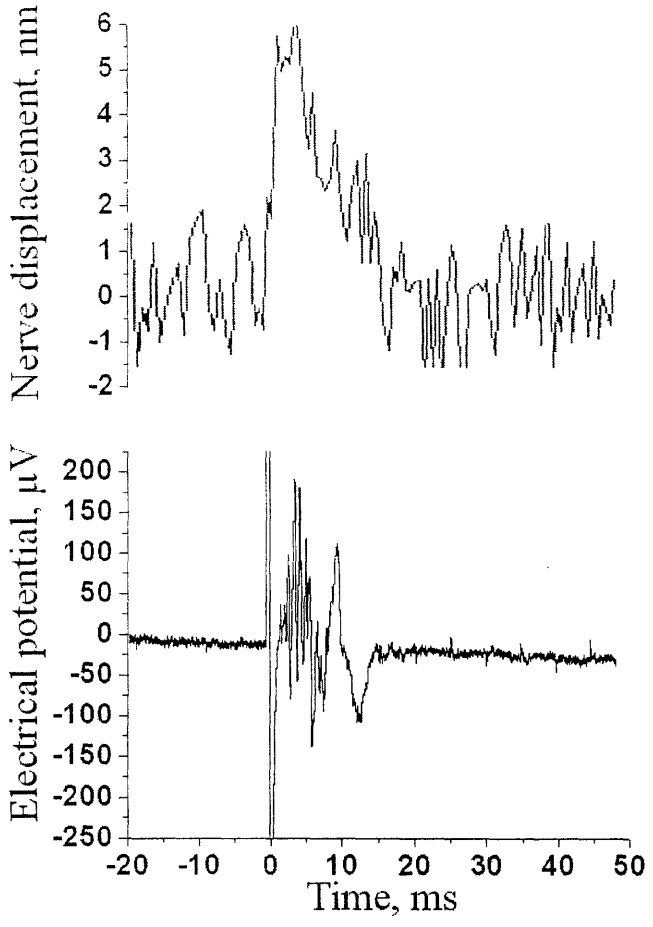

Figure 4-8: Nerve displacement and electrical potential of the nerve bundle during a 4mA stimulation. Positive displacements correspond to an increase in height of the nerve bundle surface. Electrical plot shows a stimulus artifact followed by compound potential from different axons in the bundle.

The duration of the swelling is usually 10-20ms FWHM.

4.3.3 Threshold experiment

In the previous section, we showed that our interferometer measured a displacement of the nerve bundle surface during a stimulation. However, this swelling might not be associated with the action potential. There are thermal effects on the nerve during stimulation. [21] Perhaps the interferometer is picking up artifacts from the them or from the disturbance of the surrounding solution when the stimulated electrodes are activated.

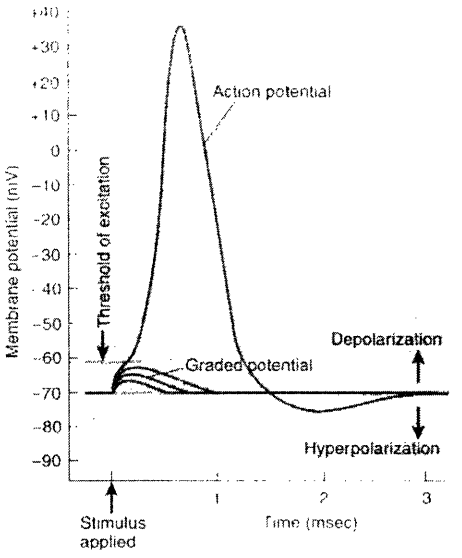

Figure 4-9: The action potential

An experiment was done to rule out such artifacts. A nerve was placed in the same chamber and setup as before. (Figure 4-2, 3-5) The amplitude of the pulse was varied from 0-10mA in 0.5mA/second intervals. One second gives enough time for the nerve to recover from its previous action potential. The full result of this study is included in Appendix B.

Figure 4-10 plots the summary of the experiment. For this graph, we have taken the peak electrical potential and the peak displacement for each stimulation current. Both the electrical and the displacement data follows the similar sigmoidal shape. They both have the same threshold current ($\approx$ 1.5 mA) and the same saturation current ($\approx$ 5 mA). This would seemingly rule out any thermal effects, since we would not expect any thermal expansion pattern to follow the same saturation pattern as the action potential.

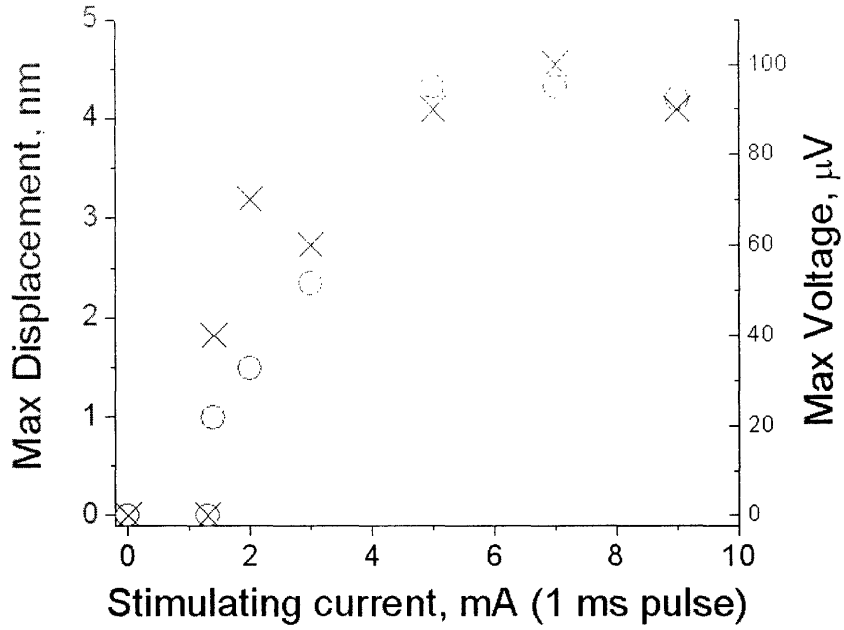

Figure 4-10: Data from a single nerve with a variable stimulus current. Circles represent peak displacements and crosses represent the peak electrical potential of the nerve.

4.4 Discussion

We have demonstrated that using the optically referenced low coherence heterodyne interferometer, we are able to measure the nanometer physical changes that accompany the action potential for a group of axons. The optical signals we observed in electrically active neurons have the same sigmoidal shape from other electrophysiology experiments. This further suggests our conclusion that the optical phase changes measured by our interferometer correspond to the action potential of the nerve.

As far as we know, there has been no solid biophysical model for the swelling of the nerve during action potential. It has been hypothesized that Ca^{2+} influx during neural excitation could trigger a cytoskeletal rearrangement which could produce significant volume changes. However, Yao suggested that these influxes are too slow to account for the fast mechanical responses. [4]

The ability to measure these intrinsic changes of the nerves optically allows us to probe the mechanisms of these changes. In the next chapter, we will present a

modification of the system that will give a full field phase image of the sample. It will then be possible to optically monitor neural communication.

Table 4.1: Specifications of the parts used in the nerve experiment

Parts	Company and part number	Relevant specs
SLD	Optospeed sled155020a	λ_0=1550nm, FWHM=35nm
Fiber Circulator	AC Photonics	
Fiber Collimator	Koncent	
WDM	Thorlabs	630nm/1550nm
AOM	Brimrose AMF-110-1550	peak efficiency $\approx$ 75 %
HeNe laser	Melles Griot	λ_0=632nm
Stimulator	Linear Stimulus Isolator A395	I_{output}: 100μ A to 10 mA
Amplifier	World Precision Instruments DAM 50	AC gain: 100x, 1000x, 10000x

Chapter 5

DBHI probe

5.1 Introduction

In this chapter, we present a modification to the interferometer. We mentioned in the last chapter that the nerve control experiment is about 5-10 times noisier than the coverslip control experiment ($\approx 1\ \mu W$ for the nerve experiment.) Moreover, in the current interferometer design, two reflective surfaces needed to be focused at the same time. For the nerve experiment, we adjusted our optics such that the focus is on the top surface of the nerve. However, there were optical and mechanical issues. Optically, since the two surfaces are separated by a few millimeters, the coupling efficiency back to the fiber from the glass reflection is low. Mechanically, we needed to lower the reference surface mount along the cage assembly rods while maintaining the nerve alignment. The alignment turned out to be very sensitive and was very time consuming.

To address these problems, we designed a small, fiber optic unit which has an integrated referencing surface inside the probe. The probe will have a fixed reflecting surface inside which will provide the reference reflection at all times. The output light will also be focused by the probe, which will be used to illuminated the sample. Moreover, a probe will be far more versatile to manipulate. Suppose we want to do

multi-point studies on the nerve. Instead of aligning the reference glass and move the chamber each time, we would simply attach the probe to a PZT and scan the probe. Thus with the probe, it is possible to have a full field phase image of the sample by scanning the probe.

5.2 First probe: GRIN lens referencing

The first probe design used a pre-made fiber collimator with back of a GRIN lens as the reference surface. (Koncent collimator KMSC 1550) The collimator was aligned with a Plano-GRIN lens. The two were then assembled together inside an aluminum housing. Collimated light coming out of the fiber collimator will be partially reflected at the back surface of the Plano-GRIN lens. The transmitted light will be focused by the GRIN lens and directed onto the sample. Figure 5-1 shows the design of this probe.

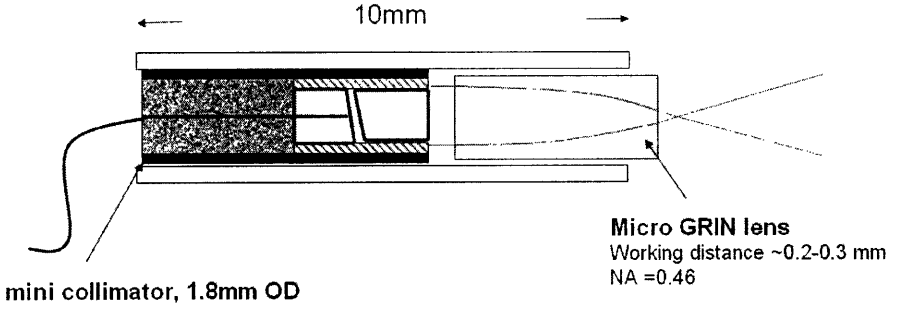

Figure 5-1: Initial DBHI Probe design.

It was difficult to align the probe so that the back reflection from the GRIN lens was coupled efficiently to the input fiber. Alignment was sensitive to angle variations, which were hard to adjust, given the mechanical housing constraints. Moreover, the collimator and the GRIN lens needed to be glued to the housing while preserving the alignment. Even with proper assembly, the alignment drifted away after a day or two. The drift was most likely due to drifts of the epoxy used. (Loctite 5 minute epoxy)

5.3 Second probe: fiber tip referencing

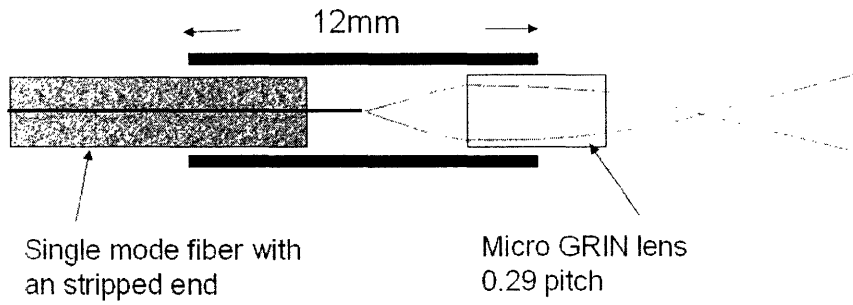

Figure 5-2: Second DBHI probe design.

We developed another method in which we used the back reflection from a cleaved single mode fiber as the reference. The fiber (Thorlabs SMF-1550) was cut and stripped down to its core. The core was then cleaved using the Thorlabs cleaver. Due to the glass/air interface, a 2-4% reflection will occur at the boundary of the core, depending on the angle of the cut. In usual fiber optics applications such as to make a connector, the fiber end is cut with an angle such that this back reflection is as small as possible (8 degrees will give -80 dB back reflection). We wanted the exact opposite. This back reflection did not need to be aligned, in the sense that there is no angle or position fine tuning involved other than the cleaving. This made it much more stable than the first GRIN reflection probe.

After the fiber was cleaved and the back reflection was optimized, it was then inserted into a glass ferrule. (Thorlabs 18-1103) A GRIN lens was inserted along with the ferrule into an overall glass housing that connects the two pieces. All the optical components were secured by using an UV Epoxy with 5-10 minute curing time. The position of the GRIN determined the NA of the system and the working distance. (Working distance is defined to be the distance between the outgoing end of the GRIN to the focus point) The final locations of the components were calculated

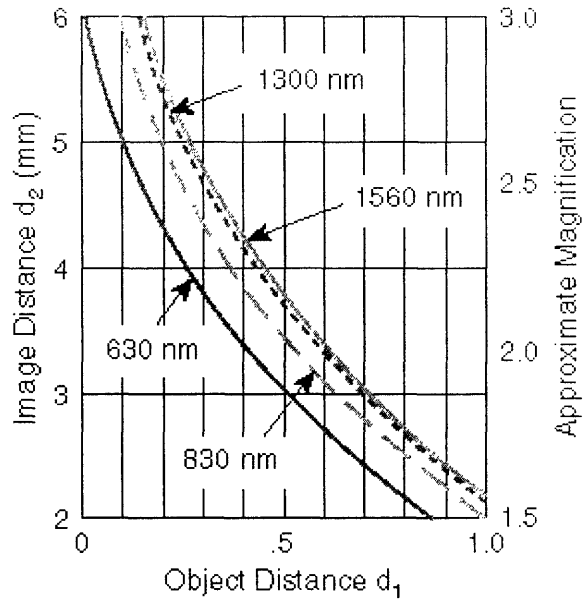

Figure 5-3: Object and Image Distance for 0.29 Pitch Lenses

using information from Figure 5-3 (from Newport Corporation).

5.4 Test data

We now present some test data from the second probe design. The experimental setup is shown in Figure 5-4. The probe was placed on a mirror mount next to a mirror which acts as our sample. The power going into the probe is 100 μW with 2-3% back reflection from the fiber tip.

The phase data taken from the experiment is shown in Figure 5-5. The experiment was much easier to set up than before. And also, as expected, the back reflection heterodyne signal has a modulation amplitude five times larger than the setup used in the nerve experiment.

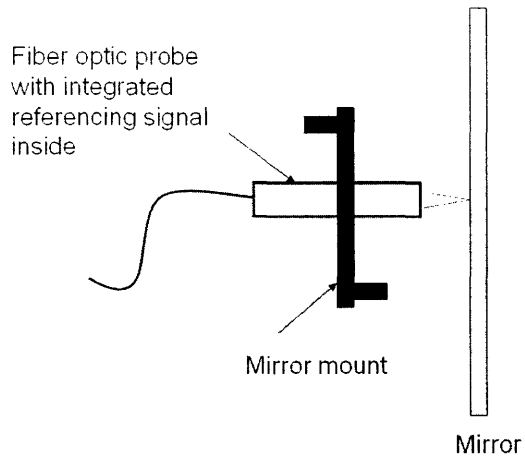

Figure 5-4: Experimental setup for testing the stability of the probe

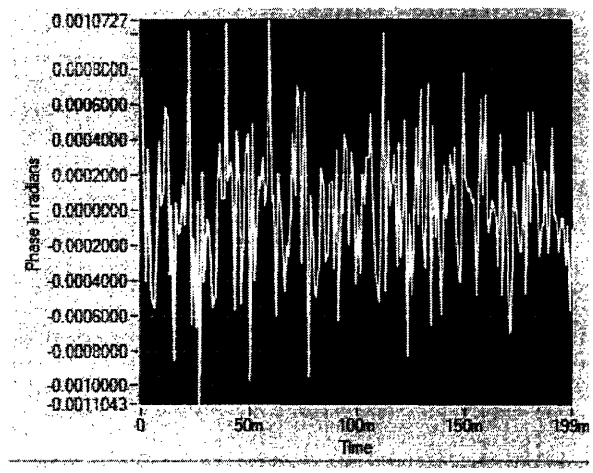

Figure 5-5: Stability of the probe. STD 0.09nm optical path length. The data was 1ms averaged.

Chapter 6

Conclusion: Future outlook and summary

6.1 Probe applications

Before development of the probe, the interferometer was mostly used to measure changes at a single point . Monitoring dynamics at different locations was not instrumentally feasible. At the time of this thesis, the DBHI probe had just been developed. The ability of the probe to access the sample at different angles and different locations makes it robust. With further development, it could be used in many different applications. Here we discuss some of the them.

1. Angle study of single axon

As discussed in Chapter 1, the origin of the swelling is still not clear. It is also unknown if the swelling preserves volume. The probe will advance the nerve displacement experiment a step further. As shown in Figure 6-1, we could map the profile of the expansion and track the propagation of the expansion of the nerve bundle undergoing an action potential. Moreover, with a better signal to noise ratio, we can do single axon studies. With a single action potential, it will be easier to separate the

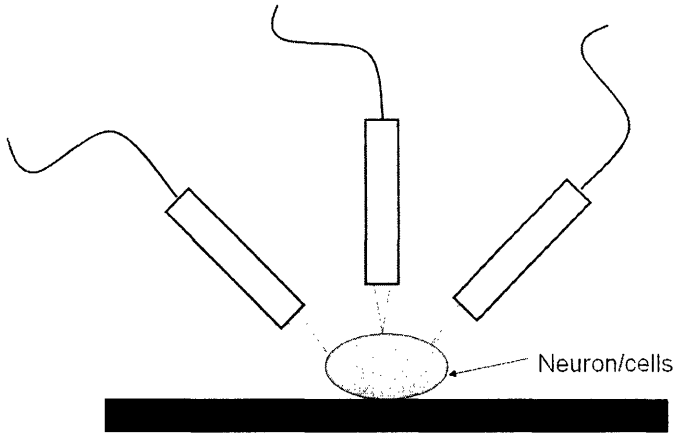

Figure 6-1: Angled study setup for nerve bundle expansion.

real intrinsic neural signal from artifacts. This could answer the question of whether the expansion is isovolumetric, and perhaps lead to insights as to the mechanisms of the expansion.

2. Imaging small neural network

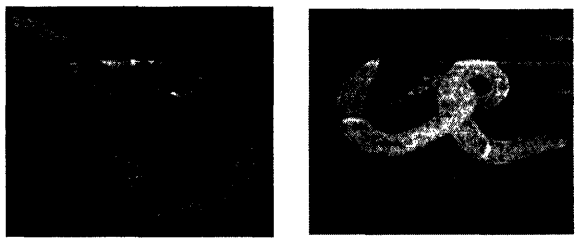

Figure 6-2: Caenorhabditis elegans

Scanning the probe enables us to ,in effect, have a phase contrast confocal microscope. Unlike phase contrast microscopy, however, the image obtained by this probe will be quantitative.

It is feasible to image a group of cultured neurons using the probe. Eventually, in-vivo imaging of small neural networks and perhaps tracking neural activities in small organisms like C. elegans should be possible. (Figure 6-2) Caenorhabditis elegans is a small (about 1 mm long) soil nematode that has been studied in biology and neuroscience because it shares many characteristics that are central problems of human

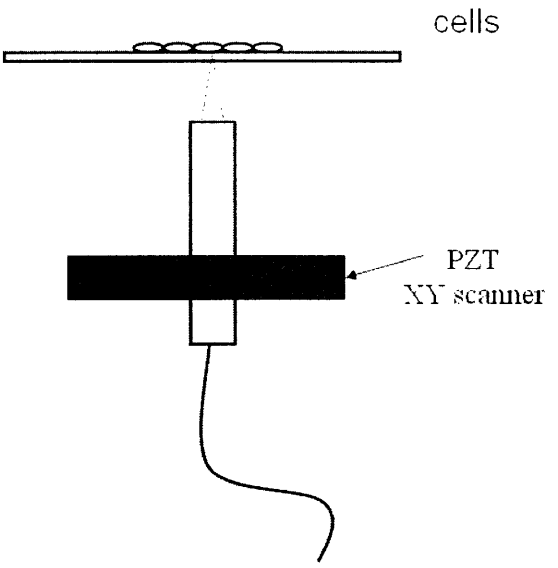

Figure 6-3: DBHI probe microscope

biology. It has a nervous system with a 'brain' and is capable of learning. C. elegans contains about 900 somatic cells and 300 neurons. The body is transparent, which makes it ideal for an optical study of its cellular and neural structure. The small neural network gives the organism sense organs in the head which mediate responses to taste, smell, temperature and touch. An instrument like our DBHI that can trace these neural activities optically would be very valuable.

3. Mechanisms of hearing transduction

The remarkable sensitivity of mammalian hearing results from the ability of inner ear sensory receptor cells to generate mechanical force in response to small electric fields. These forces can follow electrical signals up to 100 kHz and has extremely small vibrations– less than 0.35 nanometers. So far, photometric, video-enhanced, and confocal laser scan microscopy have been used to measure these movements. The inaccessibility of these cells makes the study even more difficult.

An optical instrument, laser-Doppler vibrometer (LDV), is often used in the vibration measurement. The vibration of the organ of Corti, a three-dimensional microme-

chanical structure that incorporates the sensory cells of the hearing organ, was measured in three mutually orthogonal directions using laser-Doppler vibrometer (LDV).

With the probe, we could investigate the micromechanics of the cochlear partition and identify the different modes of vibration. The probe could access the apical part of the cochlea, where the surface of the organ of Corti is optically accessible. Since the probe can detect nanometer changes at kHz speed, it is well suited to such study.

4. Glaucoma

Glaucoma is a group of eye diseases that damages the retinal nerve fiber layer (RNFL) and can result in vision loss if untreated. [12,14,15] In early stages of glaucoma, retinal nerves loses some of their functionality before cell death. The damaged nerve will thin out and cannot create and propagate action potentials effectively. Various methods are used to diagnose glaucoma. Two widely used methods are to measure high levels of intra-ocular pressure and to measure the sensitivity of the peripheral visual field. OCT is also being used to study the thinning of the RNFL and the loss of birefringence. It has been postulated that the loss of birefringence of nerve fibers is a sign of early glaucoma.

If the probe could monitor action potentials optically, it could be used to characterize the functionality of stimulated retinal nerves.

6.2 Summary

In this thesis, we have introduced a novel low coherence interferometer. The dual beam heterodyne interferometer uses a low coherence light source to measure phase changes of the sample. The optical referencing method corrects for phase noise in the interferometer and allows sub-nanometer optical path length change measurements. We showed in a proof of principle experiment that the interferometer was indeed measuring the phase. We also showed that the phase correspond to actual physical optical changes in the sample.

For the neural-physical study, we discussed the motivation to optically measure intrinsic changes of an electrically stimulated nerve. In Chapter 4, we showed the ability to measure sub-nanometer neural displacements during action potential with a single shot (ie. no signal averaging). As far as we know, this is the first non-contact optical study of such effect without introducing chemicals or reflection coatings. From the threshold experiment, the data strongly suggest that the swelling is action potential induced. Thus, this instrument is a valuable tool for studies of non-invasive neural dynamics.

In Chapter 5, we demonstrated an upgrade of the system by designing a probe at the sample end. Currently, we are perfecting the probe. The probe can image phase with precisions better than the data presented in the nerve experiment due to better signal to noise ratio and a better optical design. The robustness of the probe will allow us to study small neural networks both in-vivo and in-vitro.

6.3 Concluding remarks

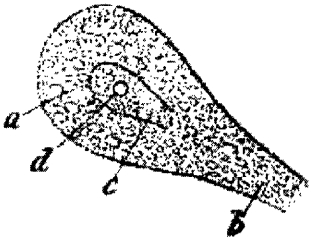

Figure 6-4: Drawing of a neuron by Gabriel Valentin, showing the protoplasm (a), the nucleus (c), the nucleolus (d) and the axonal cone (b).

The study of the brain has long fascinated scientists and philosophers. Descartes felt that the flow of the blood from the heart to the brain served the purpose of producing "animal spirits" which animated the body. In 1836, Valentine first discovered individual nerve cells, or neurons. Since then, advances in neural understandings were largely driven by technological advances. First, the invention of the achromatic microscope allows smaller structures, such as dendrites and axons, to be seen. Then with

the Golgi's staining technique, key neural dynamics were discovered. (Dendrites and axons stem from neurons: neurons do not fuse together.) Finally, with the advent of electrophysiological technique and the electron microscope, different neural potentials and neuraltransmitters were discovered. It is our hope that this DBHI interferometer will also enable present neuroscientists to advance over previously enigmatic plateaus.

Appendix A

Labview codes

A.1 dualbeam-control.vi

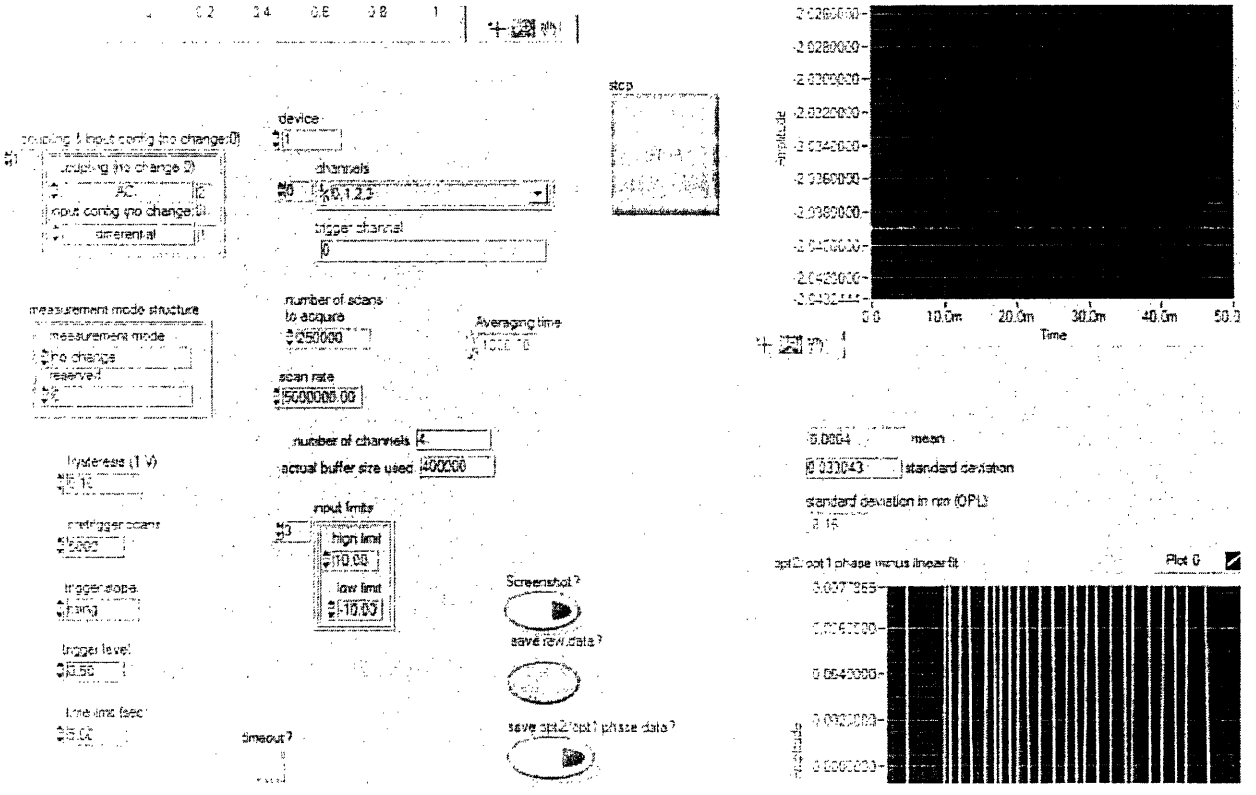

Figure A-1: Panel control for the dual beam interferometer.

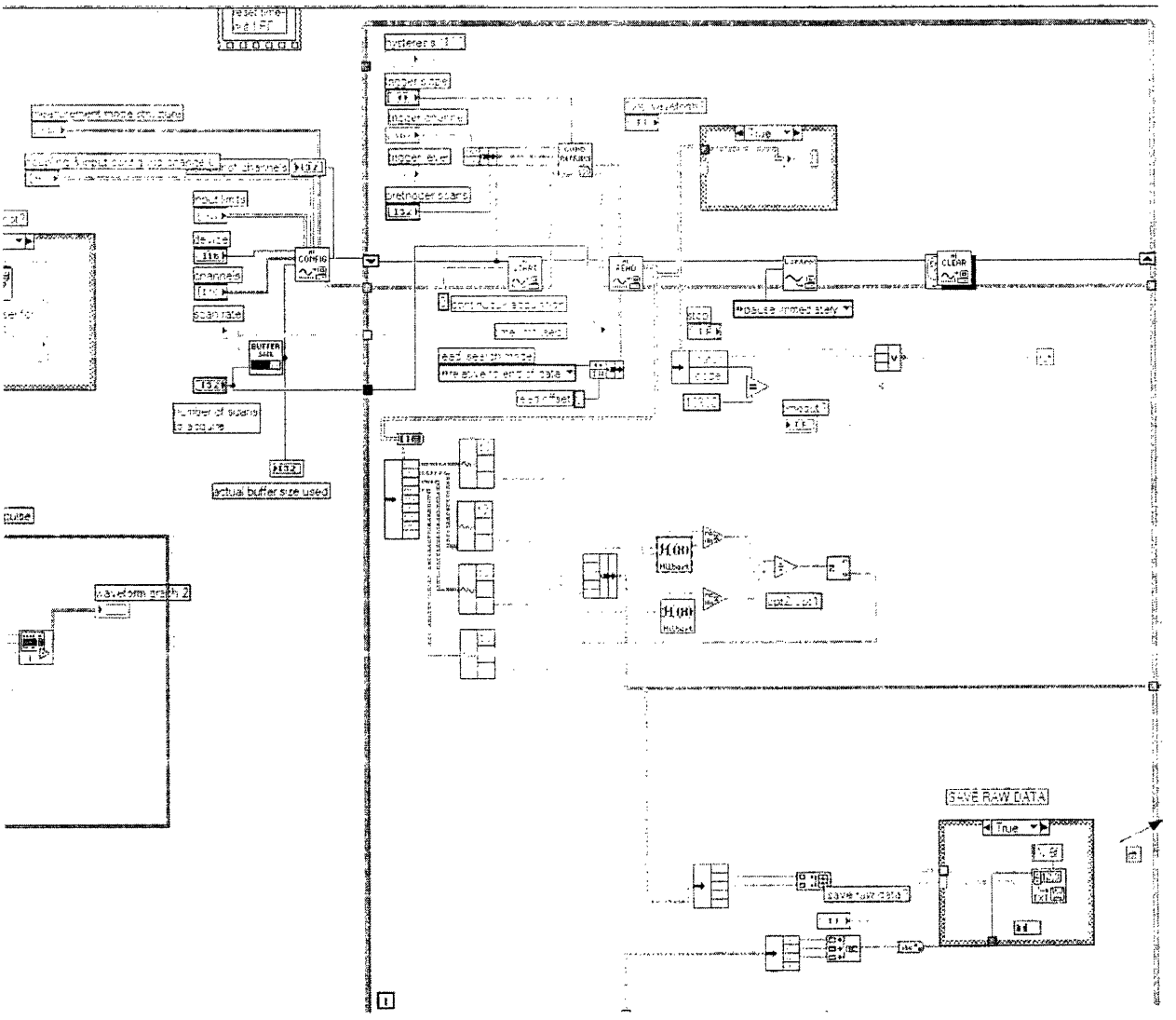

Figure A-2: dualbeamdata.vi: collect, extract the phase, and output the data in realtime. (partI)

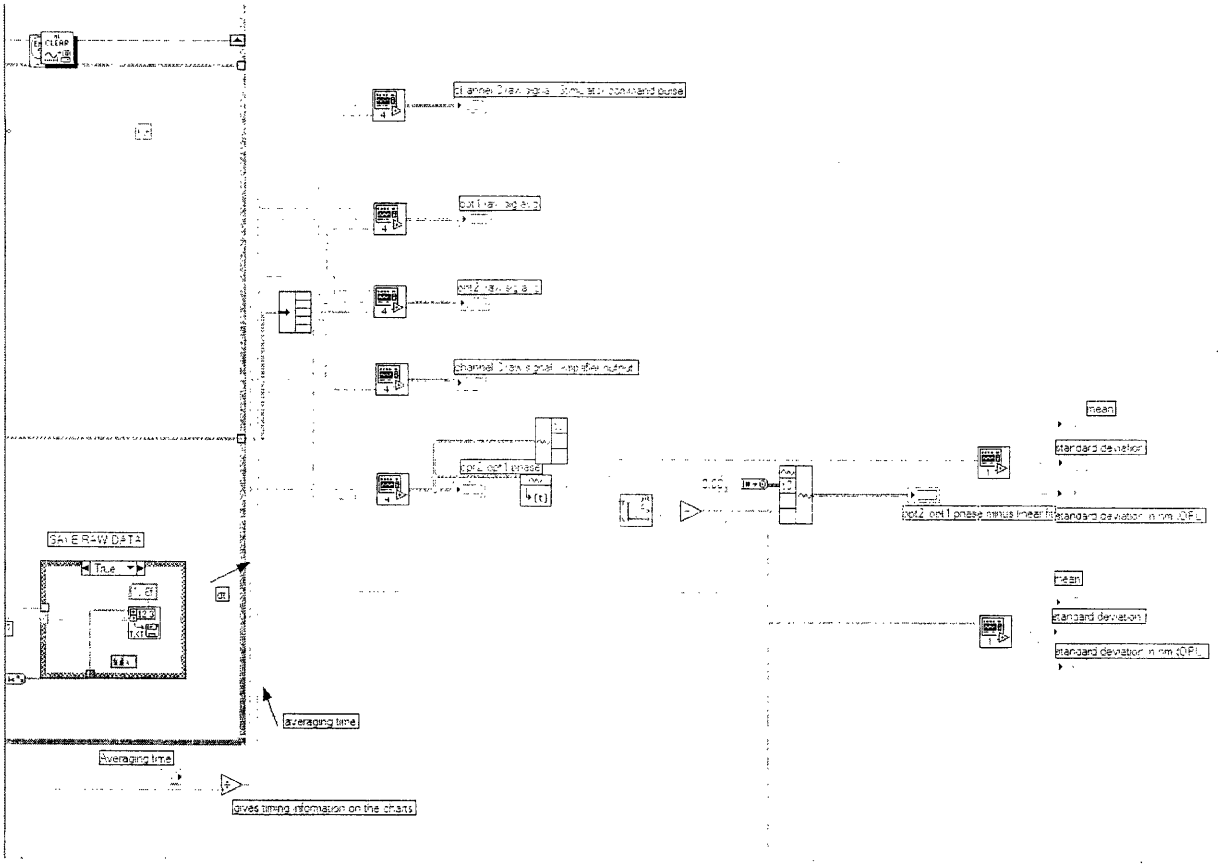

Figure A-3: dualbeamoutput.vi: collect, extract the phase, and output the data realtime. (partII)

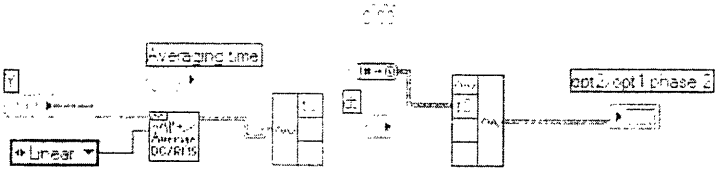

Figure A-4: time average the data points and display its phase information.

A.2 scanning.vi

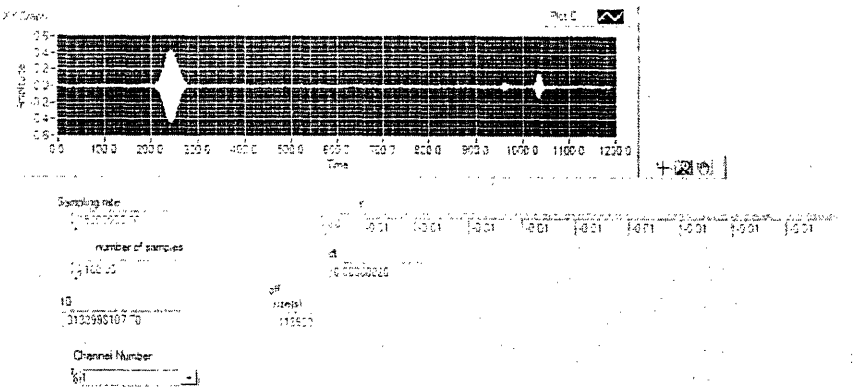

Figure A-5: Panel control for the scanning.vi

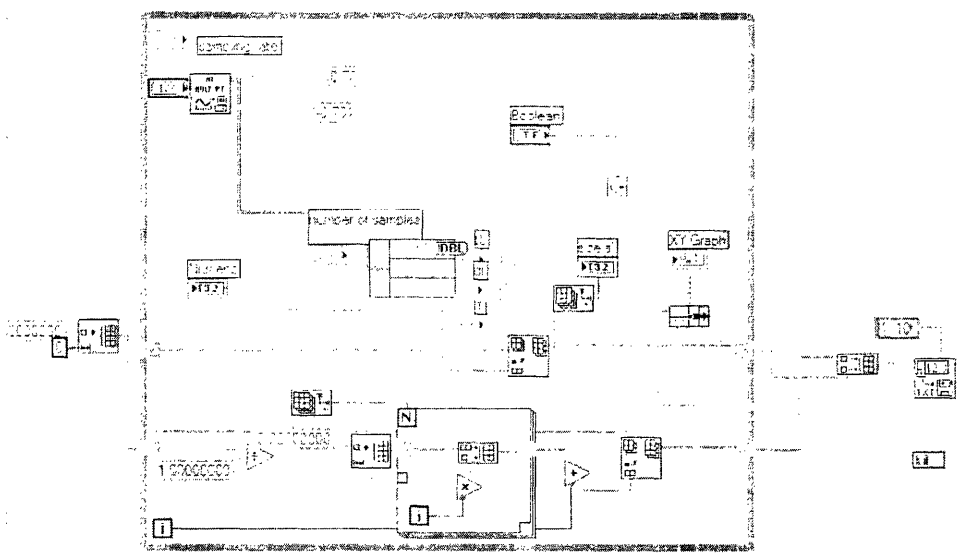

Figure A-6: scanning.vi: scans the interferometer arm and takes amplitude data.

A.3 pulsed-output.vi

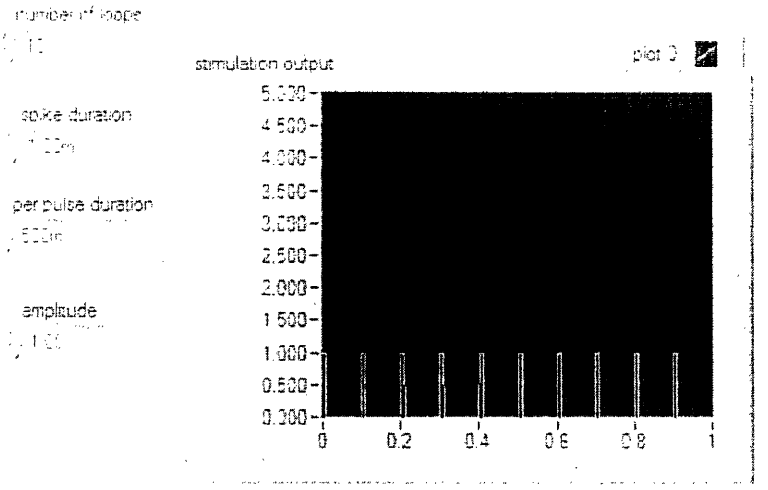

Figure A-7: Panel control for the pulse stimulation output.

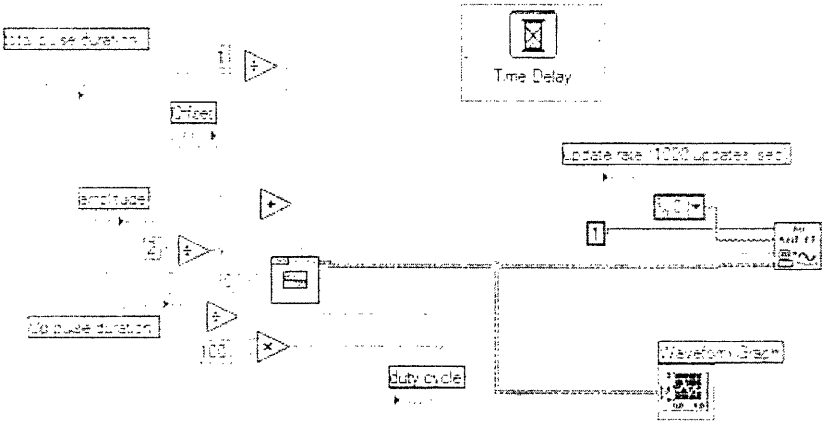

Figure A-8: pulsed.vi: a subvi that creates a controllable output voltage pulse. It can change both the duration of the pulse and its amplitude.

A.4 Hilbert-mod.vi

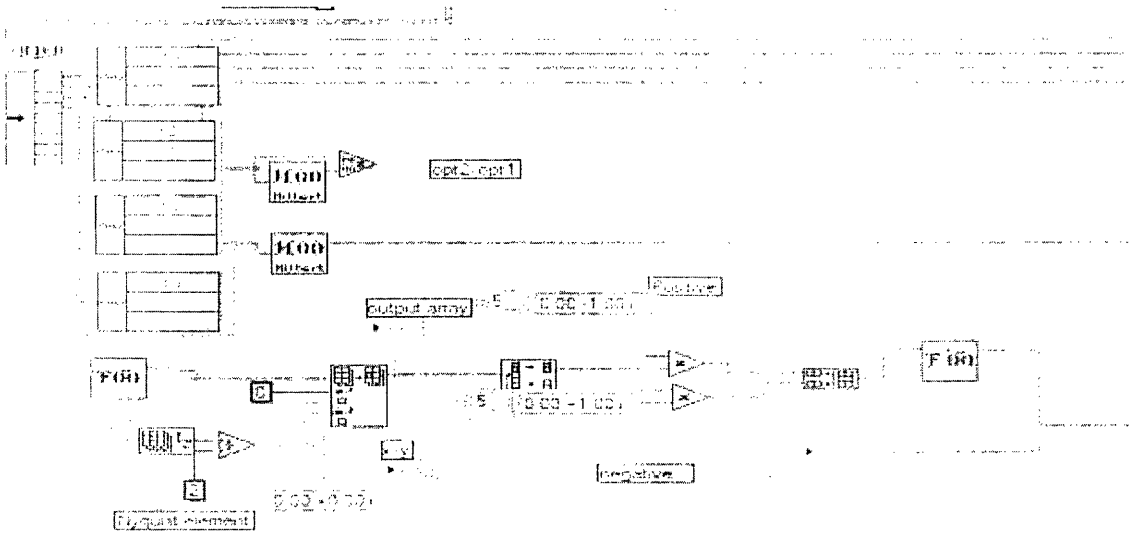

Figure A-9: Another way of doing the Hilbert transform by using the point by point Fourier transforms.

Appendix B

Nerve displacement and action potential data

Here we include the raw data taken from the threshold experiment. The first two graphs below shows the typical stimulus current and the raw phase data taken with the drift. The drift is taken out for all the subsequent figures.

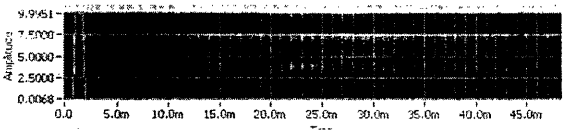

Figure B-1: Stimulation square pulse

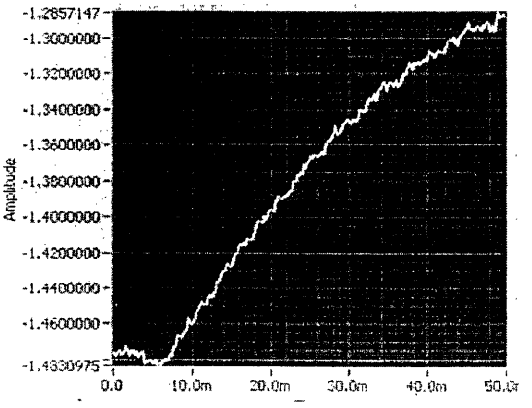

Figure B-2: Raw phase data of the nerve. Increasing phase in the graph correspond to a decrease in OPL.

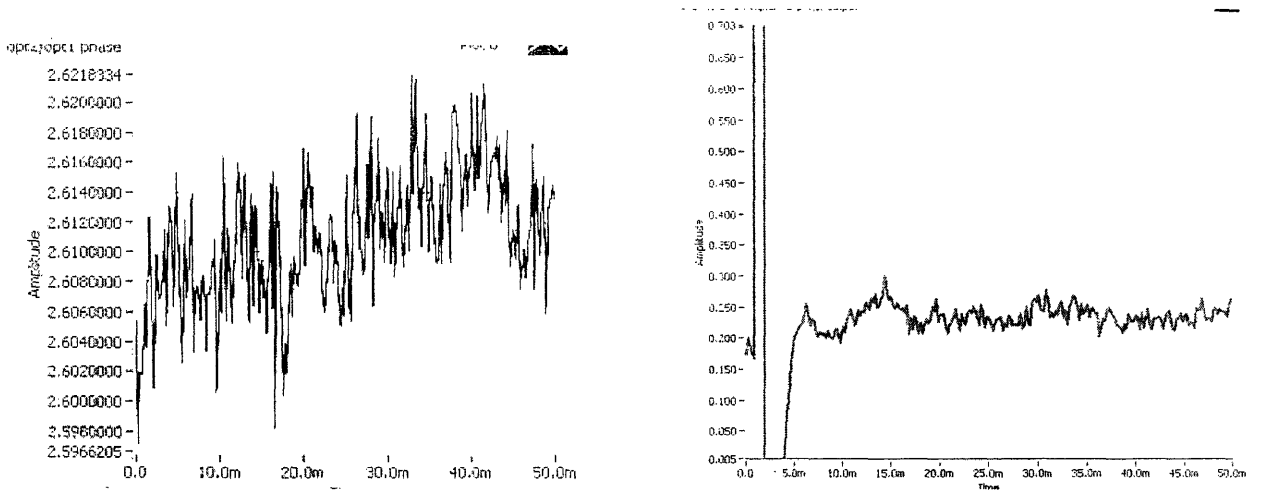

Figure B-3: Stimulation current = 0.1mA. Phase data on left; electrical potential on right.

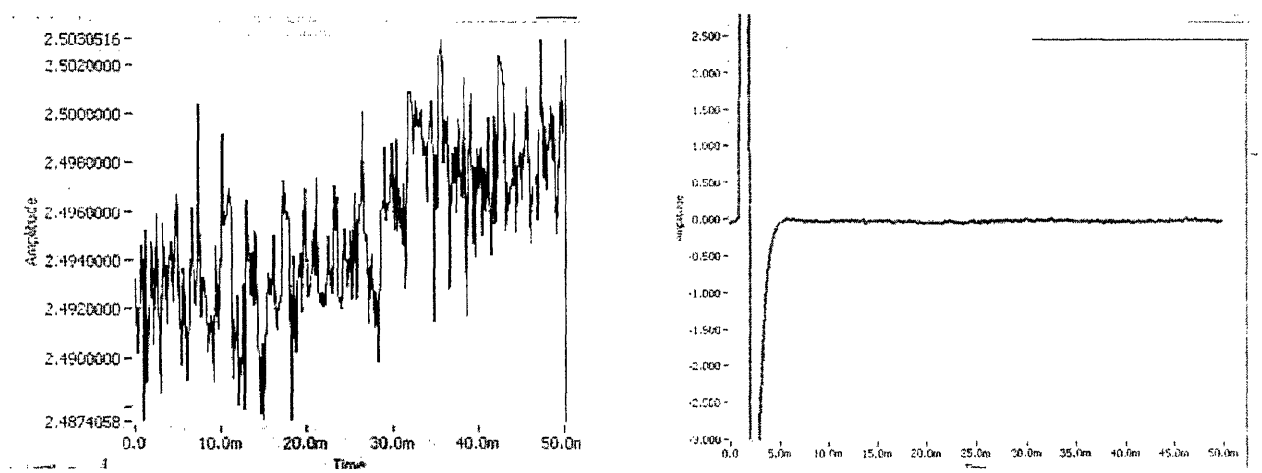

Figure B-4: Stimulation current = 1mA. Phase data on left; electrical potential on right.

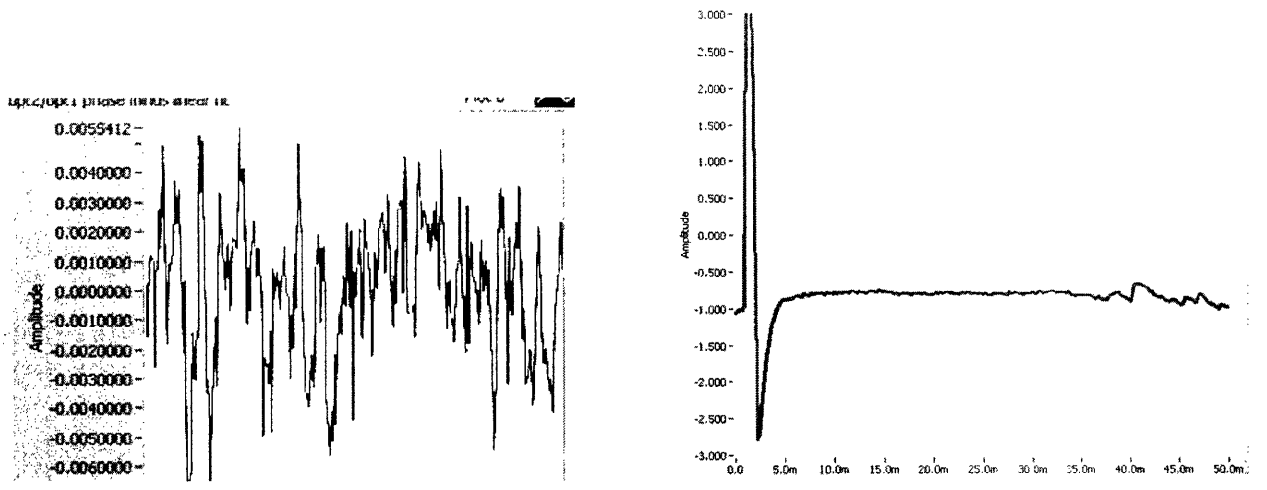

Figure B-5: Stimulation current = 1.2mA. Phase data on left; electrical potential on right.

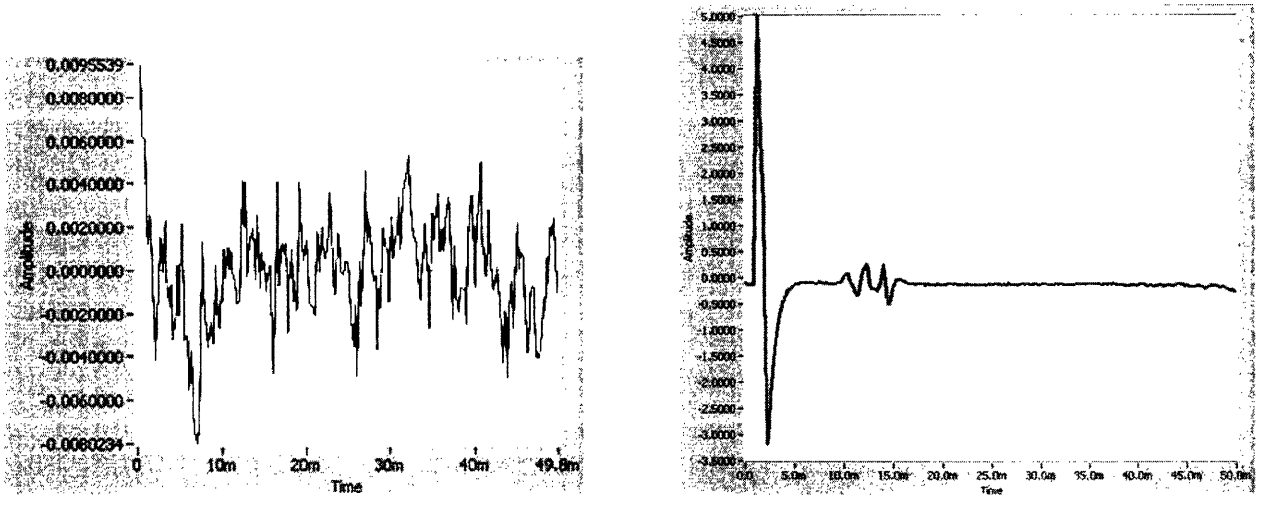

Figure B-6: Stimulation current = 1.4mA. Phase data on left; electrical potential on right.

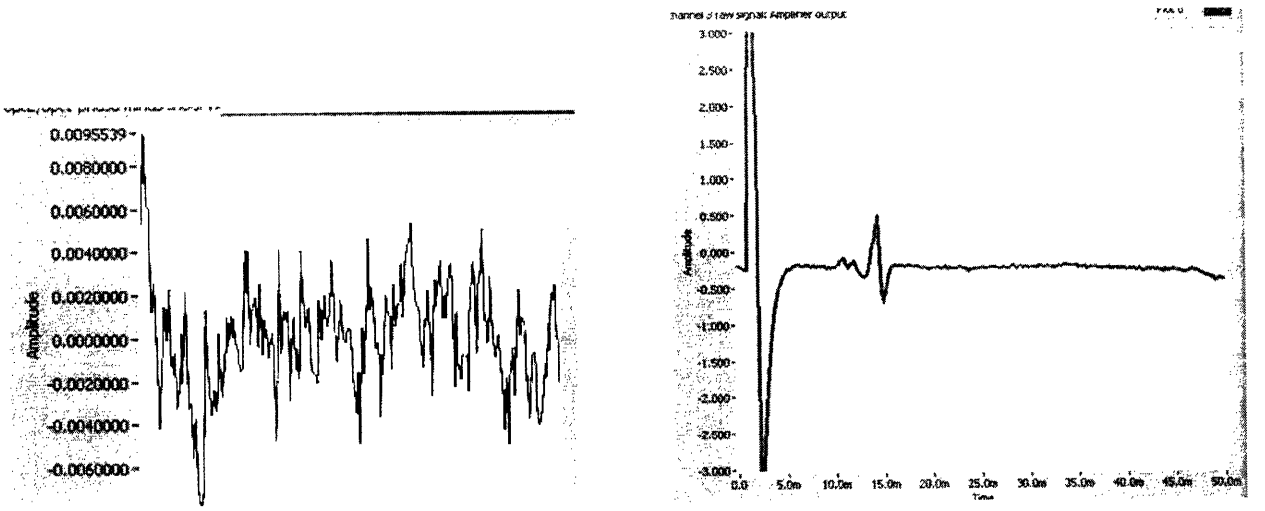

Figure B-7: Stimulation current=1.6mA. Phase data on left; electrical potential on right.

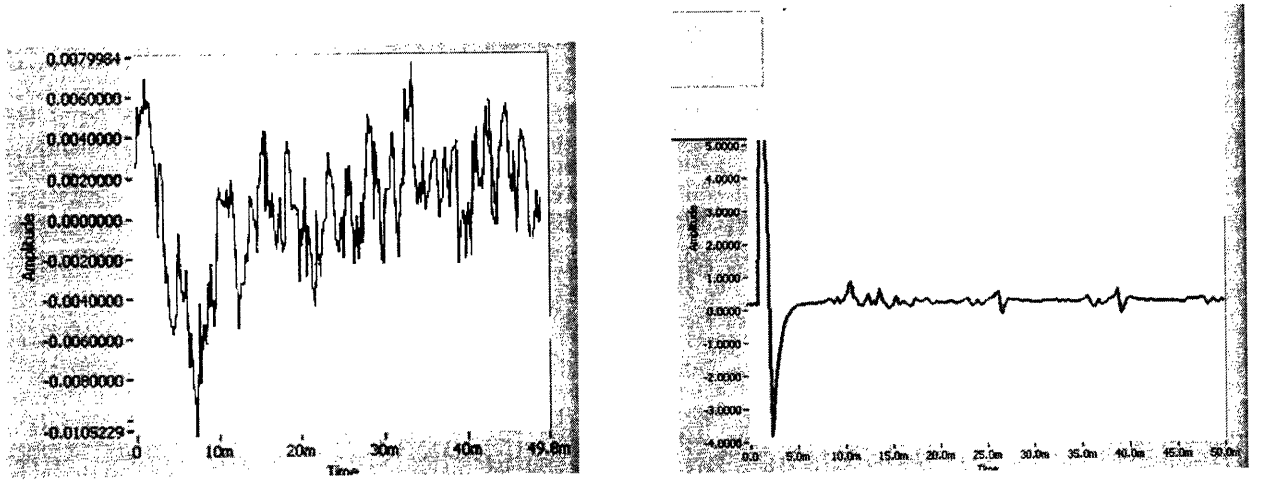

Figure B-8: Stimulation current = 2mA. Phase data on left; electrical potential on right.

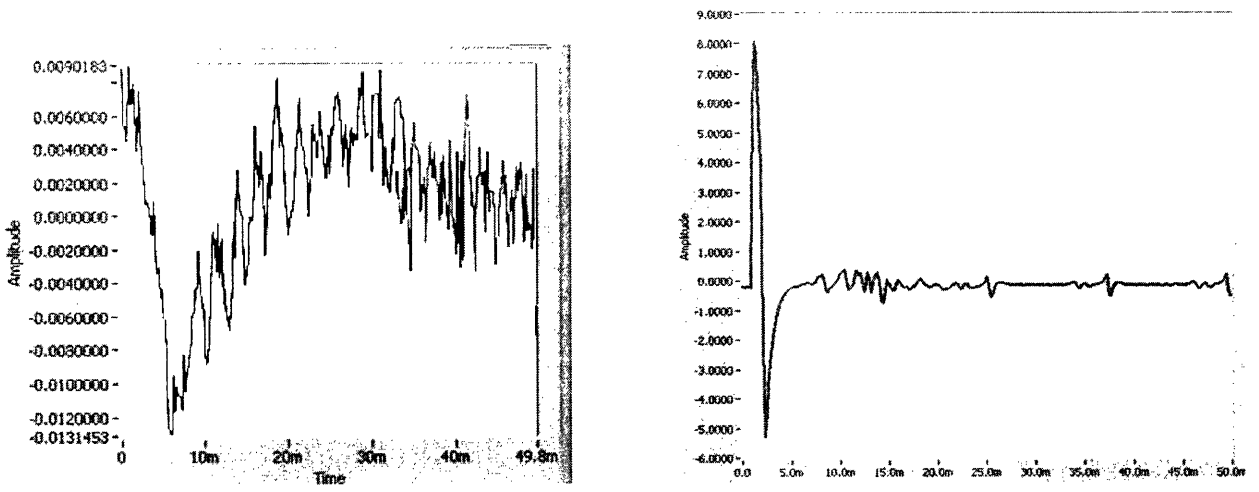

Figure B-9: Stimulation current = 3mA. Phase data on left; electrical potential on right.

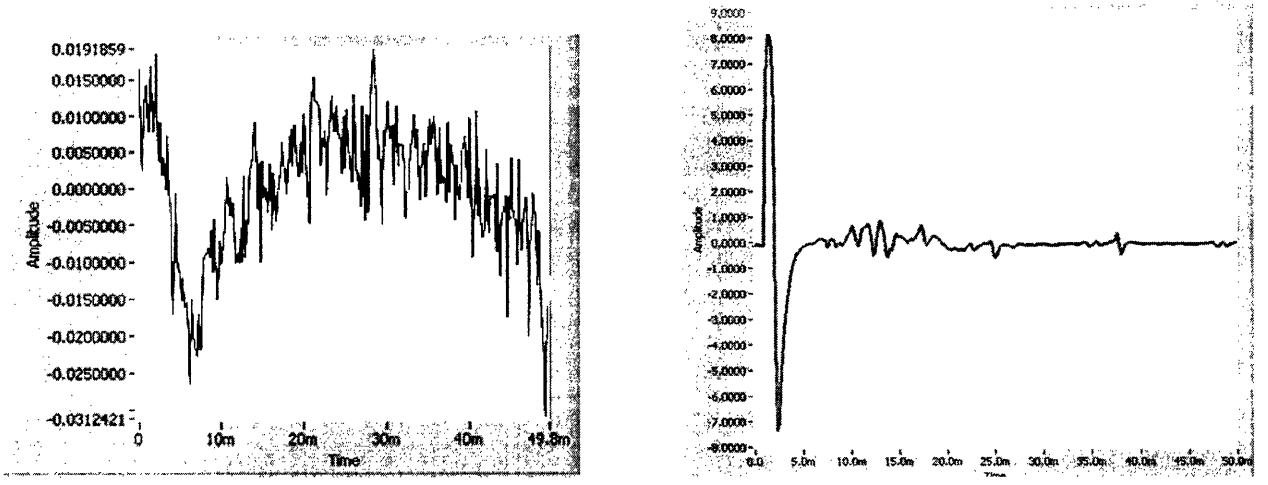

Figure B-10: Stimulation current = 4mA. Phase data on left; electrical potential on right.

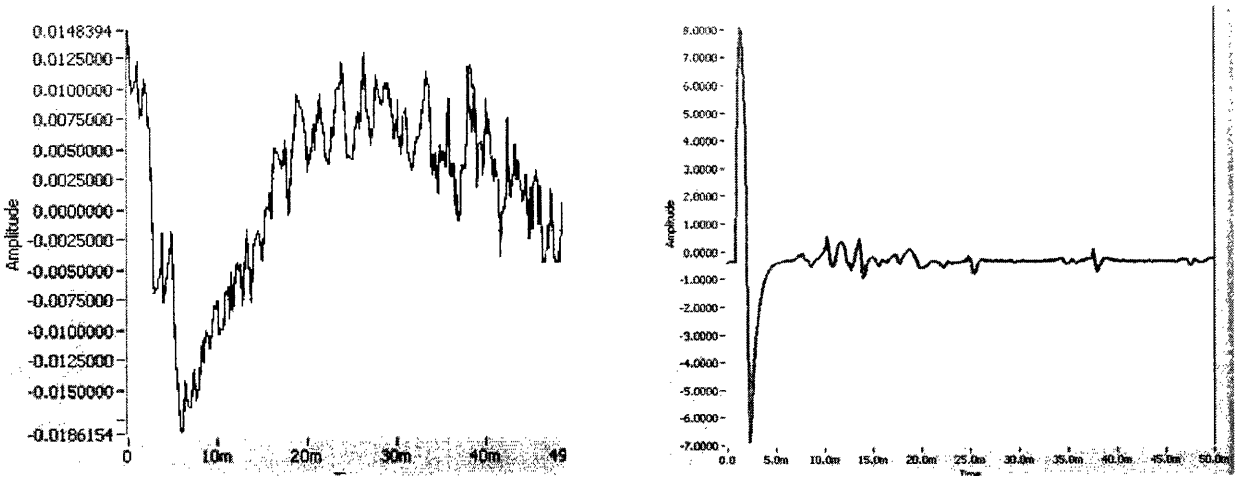

Figure B-11: Stimulation current = 6mA. Phase data on left; electrical potential on right.

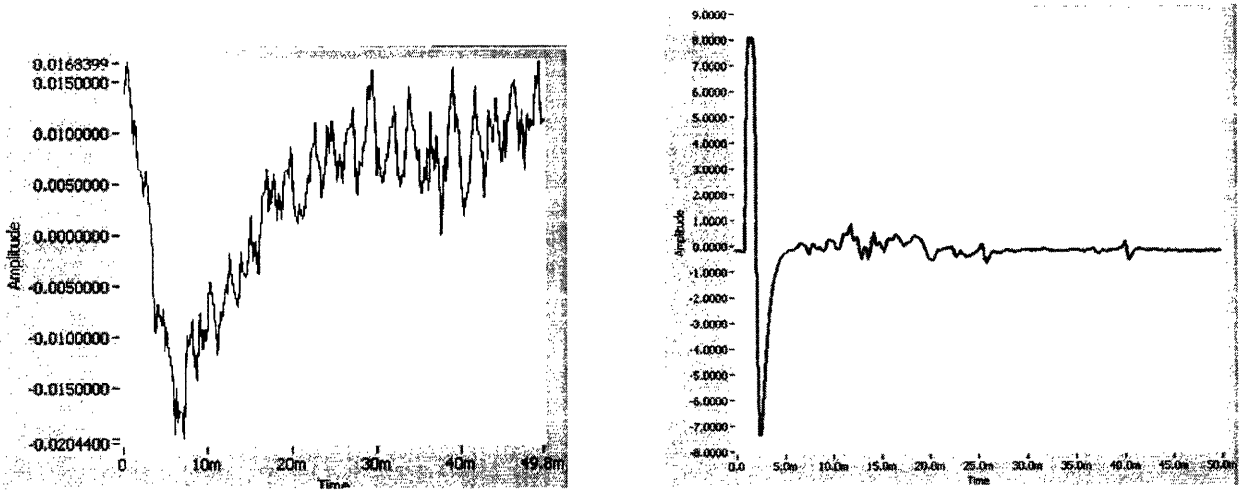

Figure B-12: Stimulation current = 7mA. Phase data on left; electrical potential on right.

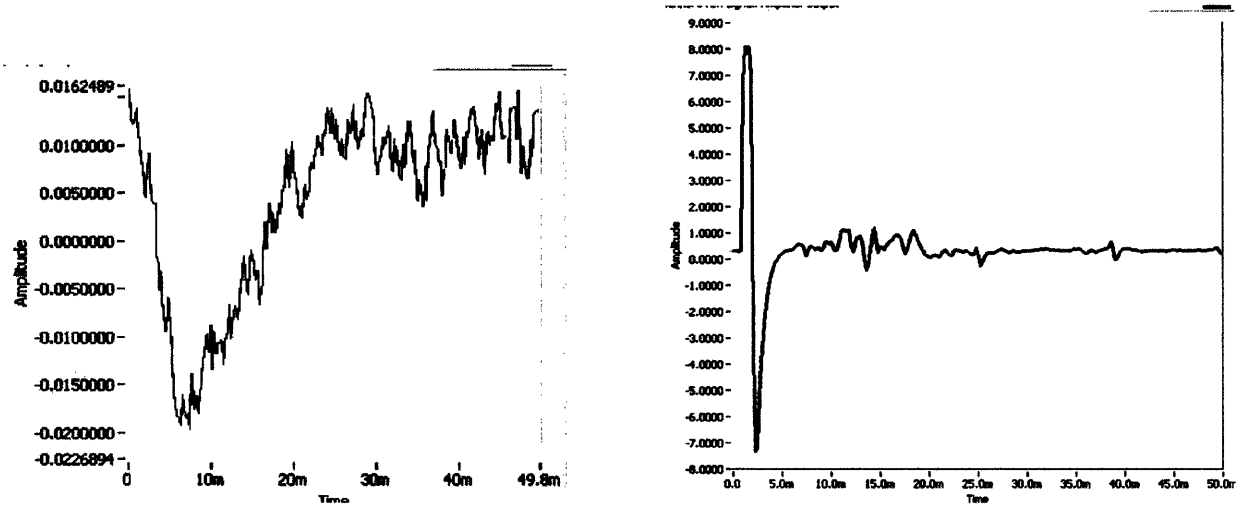

Figure B-13: Stimulation current = 8mA. Phase data on left; electrical potential on right.

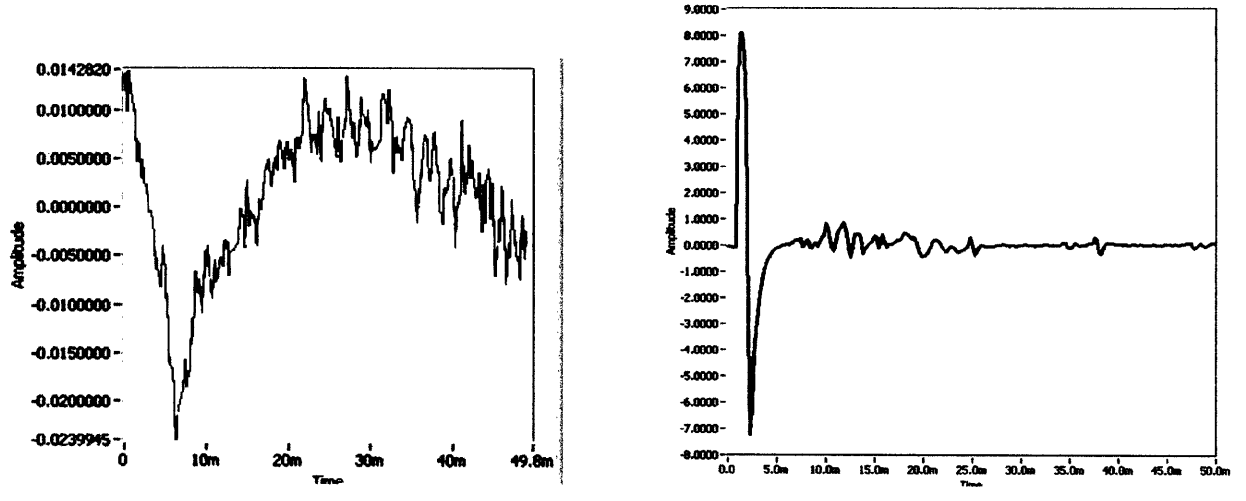

Figure B-14: Stimulation current = 9mA. Phase data on left; electrical potential on right.

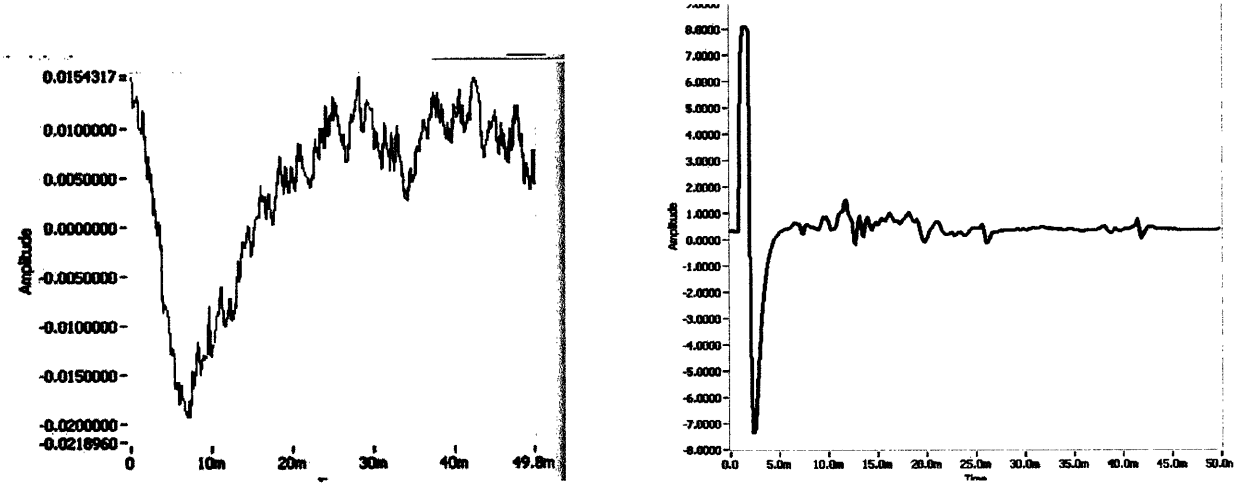

Figure B-15: Stimulation current = 10mA. Phase data on left; electrical potential on right.

Bibliography

[1] D.K. Hill, "The volume change resulting from stimulation of a giant nerve fibre," J. Physiol. 111,304-327 (1950)

[2] K. Iwasa, and I.Tasaki, "Mechanical changes in squid giant axons associated with production of action potentials," Biochem. Biophysic. Res. Comm. 95, 1328-1331 (1980)

[3] R.A. Stepnoski, A. LaPorta, F. Raccuia-Behling, G.E. Blonder, R.E. Slusher, D. Kleinfeld, "Noninvasive detection of changes in membrane potential in cultured neurons by light scattering", Proc. Natl, Acad. Sci. Vol. 88, pp.9382-9386 (1991)

[4] Xin-Cheng Yao, David M Rector, John S. George, "Optical lever recording of displacements from activated lobster nerve bundles and Nitella internodes, Applied Optics, Vol. 42, No 16 (June 2003)

[5] David Kleinfeld, Arthur LaPorta, "Detection of Action Potentials in Vitro by Changes in Refractive Index", Light Scattering Imaging of Neural Tissue Function, (2003)

[6] M. Lazebnik, D. L. Marks, K. Potgieter, R. Gillette, and S.A. Boppart, "Functional optical coherence tomography for detecting neural activity through scattering changes," Opt. Lett. 28, 1218-1220 (2003)

[7] S. H. Bryant, and J.M. Tobias, "Optical and mechanical concomitants of activity in carcinus nuerve I. Effect of sodium azide on the optical response II. Shortening of the nerve with activity," J.Cell. Comp. Physiol. 46, 71-95 (1973)

[8] I. Tasaki, Toshio Nakaye, Paul M. Byrne, "Rapid Swelling of neurons during synaptic transmission in the bullfrog sympathetic ganglion", Biochem. Biophys. Res. Commun. 188, 559-564(1992)

[9] K. Iwasa, I. Tasaki, and R.C. Gibbons, "Swelling of nerve fibers associated with action potentials," Science 210, 338-339 (1980)

[10] I. Tasaki and K. Iwasa, "Further studies of rapid mechanical changes in squid giant axon assocaited with action potential production," Jpn. J. Physio. 32, 505-518 (1982)

[11] T. Akkin, D.Dave, T. Milner and H. Rylander, "Detection of neural activity using phase-sensitive optical low-coherence reflectometry", Optics Express. 2377 vol.12, No. 11(2004)

[12] I. Tasaki, K. Kusano, and P.M. Byrne, "Rapid mechanical and thermal changes in the garfish olfactory nerve associated with a propagated impulse," Biophysical J. 55, 1033-1040 (1989)

[13] I. Tasaki, and P.M. Byrne, "Volume expansion of nonmyelinated nerve fibers during impulse conduction," Biophysical J. 57, 633-635(1990)

[14] J.A. Izatt, M.D. Kulkarni, K. Kobayashi, M.V. Sivak, J.K. Barton, and A.J. Welsh, "Optical coherence tomography for biodiagnostics," Opt. Photon. News, vol. 8, pp.41-47 (1997)

[15] J. G. Fujimoto, M.E. Brezinski, G.J. Tearney, S.A. Boppart, B.E. Bouma, M.R. Hee, J.F. Southern, E.A. Swanson, "Optical biopsy and imaging using optical coherence tomogrpahy", Nature Med, vol 1, pp. 970-972 (1995)

[16] He DZZ Relationship between the development of outer hair cell electromotility and different innervation: A study in cultured organ of Corti of neonatal gerbils. J Neurosci 17, 3634-3643 (1997)

[17] He DZZ, Jia SP and Dallos P Mechano-electrical transduction of adult outer hair cells studied in a gerbil hemicochlea. Nature (2004)

[18] L.B. Cohen, R.D. Keynes, "Changes in light scattering associated with the action potential in crab nerves," J. Physiol. (Lond) 212, 259-275 (1971)

[19] L.B. Cohen, R.D. Keynes,L. Landowne "Changes in light scattering that accompany the action potential in squid giant axons: potential-dependent componenets," J. Physiol. (Lond) 224, 701-725 (1972)

[20] I. Tasaki, P. M. Byrne, "Thermal and mechanical responses of the amphibian skin to nerve stimulation," Jpn. J. Physiol. 41, 576 (1991)

[21] I. Tasaki, P. M. Byrne, "Demonstration of heat production associated with spreading depression in the amphibian retina," Biochem. Biophys. Res. Commun. 172, 293-297(1991)

[22] J. M. Schmitt, A. Knuttel, R.F. Bonner, "Measurement of optical properties of biological tissues by low-coherence reflectometry," Appl. Opt., vol. 32, pp.6032-6042 (1993)

[23] W. Clivaz, F. Marquis-Weible, R.P. Salathe, R.P. Novak, H.H. Gilgen, "High-resolution reflectometry in biological tissue," Opt. Lett., vol. 17, pp. 4-6 (1992)

[24] Ronald Bracewell, "The Fourier Transform and Its Applications 3rd ed.",McGraw-Hill Higher Education (2003)

[25] B.C. Hill, E.D. Shubert, M.A. Nokes, and R.P. Michelson, "Laser ingerferometer measruement of changes in crayfish axon diameter concurrent with action potential," Science, 196, 426-428(1977)

[26] F. Conti, I.Tasaki, and E. Wanke. "Fluorescence signals in ANS-stained squid giant axons during voltage clamp," Biophysik 8, 58-70 (1971)

[27] I. Tasaki, A. Watanabe, and M. Hallett, "Fluorescense of squid axon membrane labeled with hydrophic probes," J. Membrane Biol. 8, 109-132 (1971)

[28] http://www.afrlhorizons.com/Briefs/Mar03/OSR0209.html

[29] http://lob.epfl.ch/Jahia/site/lob/cache/offonce/pid/45967

[30] http://www.blackwellpublishing.com/matthews/channel.html

[31] http://www.mult-sclerosis.org/actionpotential.html

[32] http://www.risoe.dk/ofd/oct/Presentations/Teaching/8